Chemical Geology 605 (2022) 120968

Contents lists available at ScienceDirect

Chemical Geology

journal homepage: www.elsevier.com/locate/chemgeo

Compositional variability of San Carlos olivine

Sarah Lambart [a,*], Sarah Hamilton [a], Otto I. Lang [a]

[a] University of Utah, Department of Geology and Geophysics, MagMaX Laboratory, USA

ARTICLE INFO

Editor: Catherine Chauvel

Keywords:
Olivine
non-USNM San Carlos
starting material
major elements
trace elements
pyroxenite
phosphorus

ABSTRACT

Forsterite (Fo)-rich olivine compositions from San Carlos (Arizona, SW USA) are commonly used as starting material in experimental petrology. In comparison to the San Carlos reference material USNM 111312/444, it has been shown that the major element variability of non-USNM San Carlos olivine is significant. We complement the characterization of the compositional variability of the non-USNM San Carlos olivine with new data, including minor and trace element analyses. High precision analyses reveal that selected minor elements (e.g., ~6% NiO, ~10% MnO, ~16% CaO, relative) and trace elements (e.g., ~75% Cr, ~120% Cu, ~160% P and Ti, relative) present significant concentration variations between grains. At the scale of the individual grain, however, San Carlos Fo-rich olivines appear homogeneous with no systematic core-rim variations. We also discuss the origin of olivine pyroxenites associated with the peridotite xenoliths and argue that they are derived by melt-rock reaction resulting in olivine dissolution and pyroxene precipitation from the peridotite host. Further segregation and in situ crystallization of the hybrid residual melt can produce Fe-rich olivine-poor pyroxenites. Finally, we discuss the origin of the P variability in San Carlos mantle olivine and suggest that P enrichment by metasomatism implies a highly reactive process with fast dissolution-reprecipitation of solid phases.

1. Introduction

Olivine is a continuous solid solution between the two main end-members forsterite (Mg_2SiO_4) and fayalite (Fe_2SiO_4). The only elements present at minor levels in mantle olivine (i.e., >1000 ppm and < 1 wt%) are Ni and Mn (e.g., De Hoog et al., 2010; Demouchy and Alard, 2021; Wang et al., 2021). However, olivine crystal defects (vacancies in particular) can incorporate a large range of elements from heavy (U, Th) to light elements (H, Li, He) (Demouchy and Alard, 2021 and references therein).

Natural forsterite (Fo)-rich olivines are commonly used in scientific research. Many electron microprobe labs use the San Carlos reference material USNM 111312/444 (Jarosewich et al., 1980) or the NMNH-distributed sample 111312/44 for calibrations. Non-USNM-distributed crystals of San Carlos olivine are also available commercially and often used as starting material in experimental studies (e.g., Grant et al., 2016; Kinzler and Grove, 1992; Su et al., 2018; Wang and Gaetani, 2008) and occasionally as "in-house" standard for analytical calibrations (e.g., Bussweiler et al., 2019; Demouchy and Alard, 2021; Rasmussen et al., 2020). The potential inherent chemical variability of starting materials may affect experimental or analytical results. Additionally, minor and trace elements in olivines have recently been extensively used to interpret various petrogenetic processes (e.g., Coogan et al., 2014; Foley et al., 2013; Rasmussen et al., 2020; Sobolev et al., 2005, 2007; Su et al., 2019; Wang et al., 2021; Xu et al., 2020). Hence, it is important to characterize the full chemical variability of the San Carlos olivine. Fournelle (2011) showed that the composition of the NMNH San Carlos reference material shows only slight major element variability ($Fo_{89.6}$ to $Fo_{90.5}$), but that non-USNM San Carlos olivine can be significantly more variable, with Fo contents (i.e. Mg/(Mg + Fe) *100) ranging from 87 to 92%. Compositional heterogeneity of olivine from xenoliths from the San Carlos volcanic field was also reported for major elements by Frey and Prinz (1978) and Galer and O'nions (1989). In our paper, we report new major, minor and trace analyses on both USNM and non-USMN distributed San Carlos olivines. We also briefly discuss the origin of the olivine pyroxenite xenoliths associated with the more common peridotite xenoliths, as well as the potential causes for the high variability in phosphorus observed in San Carlos olivine.

2. Geological background

The San Carlos volcanic field is one of the many late Tertiary to Quaternary centers of alkaline volcanism within the Basin and Range that bear ultramafic xenoliths. The Peridot Mesa vent produced a

* Corresponding author.
E-mail address: sarah.lambart@utah.edu (S. Lambart).

https://doi.org/10.1016/j.chemgeo.2022.120968
Received 6 January 2022; Received in revised form 13 May 2022; Accepted 1 June 2022
Available online 6 June 2022

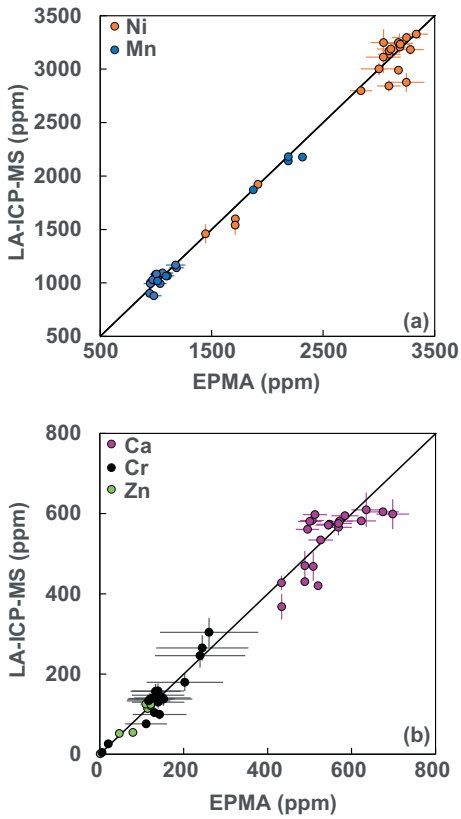

Fig. 1. Ni, Mn (a), Zn, Cr, and Ca (b) concentrations (in ppm) obtained by LA-ICP-MS and electron microprobe on a selection of olivine grains. Solid lines are 1:1 correlations. Error bars on LA-ICP-MS analyses correspond to the maximum between the one standard deviation and the analytical error. Error bars on the electron microprobe analyses correspond to the analytical errors reported in Table S1. When not visible, the error bar is smaller than the symbol.

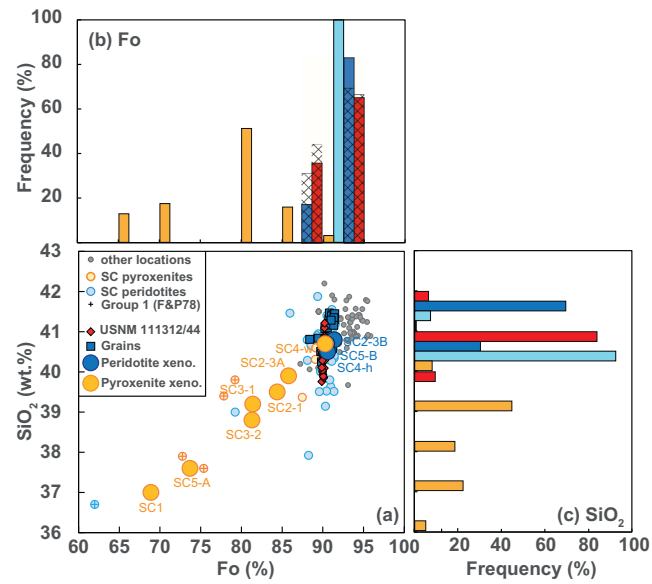

Fig. 2. (a) Forsterite (Fo) versus SiO_2 content in olivine analyzed in this study. Analyses on pyroxenite and peridotite samples represent average analyses for each sample. Analyses on grains and USNM reference material represent average analyses on individual grains. Compositions are compared to analyses performed on olivines from pyroxenite and peridotites xenoliths from San Carlos (Denis et al., 2018; Frey and Prinz, 1978; Galer and O'nions, 1989; samples identified as Group 2 by Frey and Prinz are shown with a cross) and on mantle olivines from other locations (Wang et al., 2021). (b-c) Fo and SiO_2 distributions in the four categories of SC olivines (red, USNM reference material, $n = 31$; blue, individual grains, $n = 23$; light blue, peridotite xenoliths, $n = 40$; yellow, pyroxenite xenoliths, $n = 134$). In (b), we also represented the distributions for non-USNM ($n = 1566$) and USNM ($n = 236$) olivine grains reported by Fournelle (2011; crossed area). (For interpretation of the references to colour in this figure legend, the reader is referred to the web version of this article.)

basanitic lava flow known to be particularly rich in xenoliths (Frey and Prinz, 1978). Ultramafic xenoliths from the San Carlos volcanic field are classified into two groups (Frey and Prinz, 1978; Galer and O'nions, 1989): Group 1 is more magnesian (whole-rock Mg# = MgO/(FeO* + MgO)*100 = 86–91, with FeO*, total iron) and contains Cr-rich clinopyroxenes (diopsides). Group 2 contains Al- and Ti-rich clinopyroxenes (augites) and is more Fe-rich (Mg# < 80). While Group 1 is dominated by peridotites and Group 2 is dominated by olivine clinopyroxenites, both groups contain peridotite and pyroxenite enclaves. Group 1 inclusions are usually interpreted as mantle xenoliths, residues of partial melting in the fields of garnet and spinel peridotites (e.g., Frey and Prinz, 1978; Galer and O'nions, 1989). Group 2 xenoliths appear to represent cumulates derived from silica-undersaturated magmas similar to the host basaltic lava (e.g., Frey and Prinz, 1978; Wilshire and Shervais, 1975).

3. Methods

We performed analyses on five types of olivine grains from the San Carlos (SC) Volcanic Field: (1) USNM reference material distributed by the Smithsonian Institute (USNM 111312/44 and /42), (2) small (<2 mm) olivine grains, hand-picked from an olivine sand from the SC reservation, (3) large (> 5 mm diameter) grains acquired commercially, and (4) and (5) "in situ" grains from peridotite and pyroxenite xenoliths, respectively.

Modal proportions in xenoliths from San Carlos are extremely variable (e.g., Frey and Prinz, 1978) and can change drastically on a cm-scale (e.g., Denis et al., 2018; Tilhac et al., 2021; Wilshire and Jackson, 1975). We have selected a representative set of olivine-bearing xenoliths which covers both Frey and Prinz 's Group 1 and Group 2 petrological and mineralogical diversity: SC1 is an olivine and spinel bearing clinopyroxenite; SC3–1, SC3–2 and SC5-A are olivine clinopyroxenites; SC2–1 and SC2-3A are olivine websterites; SC2-3B and SC5B are harzburgites; SC4 is a composite websterite-harzburgite sample.

We determined major and minor concentrations using an electron microprobe. Analyses were performed at the University of Utah using a Cameca SX100 and processed using the 'Probe for EPMA' software. We used two different setups for analyses: (i) one-step analyses with a 15 keV and 30 nA current using a 5um spot; on-peak counting times ranged from 20 to 30s for major elements and 60–80s for minor elements. (ii) two-step analyses during which we first analyzed the major elements at 30 nA and 15 keV using a 5um spot; on-peak counting times ranged from 20 to 30s. In subsequent analytical sessions, Ni, Mn, Al, Ca, Zn and Cr were analyzed at 25 keV with a 300 nA beam and a 10 um spot and 90 to 120 s on peak. These new data were then processed using the other element concentrations from the low beam current analyses. During each analytical session, half of the on-peak time was used on each of the high and low backgrounds. Standards used were the ASTIMEX reference standards Albite (Na), Sadinine (Al, K), Hematite (Fe), Diopside (Mg, Si, Ca), Rutile (Ti), Chromite (Cr) and Sphalerite (Zn), and the synthetic standards Ni_2SiO_4 (Ni) and Mn_2SiO_4 (Mn) provided by George Rossman. Data reduction was performed using the PAP procedure (Pouchou and Pichoir, 1991). BHVO-2g secondary standard was repeatedly analyzed during each analytical session to monitor drift on major elements (i.e., using 15 keV, 30 nA and a 10 μm spot), but no additional corrections were applied. Mean single-point analytical sensitivities and detection limits for each element are reported in Table S1.

We determined trace element concentrations on the selected grains

Table 1
Average of electron microprobe analyses on individual olivine grains.

Grain #	n[a]	SiO_2	TiO_2	Al_2O_3	Cr_2O_3	FeO	MnO	MgO	CaO	NiO	ZnO	Total	Fo[c]
smol1	4	41.17 (22)		0.02 (1)	0.01 (1)	8.97 (8)	0.12 (1)	49.29 (18)	0.07 (1)	0.42 (3)		99.9 (4)	90.73 (4)
smol2	4	41.32 (23)		0.02 (1)	0.01 (0)	8.94 (14)	0.14 (1)	49.08 (33)	0.09 (6)	0.39 (3)		99.9 (70	90.73 (18)
smol3	4	41.32 (36)		0.02 (0)	0.02 (0)	8.66 (25)	0.13 (1)	49.37 (11)	0.07 (1)	0.41 (3)		99.7 (10)	91.04 (22)
smol4	4	40.81 (20)		0.02 (0)	0.04 (6)	11.11 (14)	0.15 (2)	47.43 (22)	0.08 (1)	0.36 (3)		99.8 (6)	88.39 (16)
smol5	5	41.20 (18)		0.01 (2)	0.02 (0)	8.97 (24)	0.12 (1)	49.21 (24)	0.07 (1)	0.40 (3)		99.6 (5)	90.72 (26)
smol6	4	41.08 (25)	0.02 (0)	0.02 (1)	0.02 (1)	9.41 (13)	0.15 (2)	48.85 (26)	0.08 (2)	0.38 (4)		99.3 (4)	90.25 (13)
smol7	3	41.47 (12)		0.02 (1)	0.02 (0)	8.85 (11)	0.12 (2)	49.04 (26)	0.08 (1)	0.41 (1)		99.6 (2)	90.81 (15)
smol8	4	41.20 (30)		0.02 (1)	0.01 (0)	8.73 (28)	0.13 (1)	49.44 (33)	0.08 (1)	0.40 (2)		99.6 (3)	90.99 (30)
smol9	4	41.42 (7)		0.02 (1)	0.02 (0)	8.58 (12)	0.13 (1)	49.37 (16)	0.08 (1)	0.40 (3)		99.9 (6)	91.11 (13)
smol10	5	41.10 (30)		0.02 (0)	0.02 (1)	9.13 (11)	0.14 (2)	49.13 (24)	0.07 (1)	0.41 (2)		99.6 (7)	90.56 (9)
smol11	6	41.39 (38)		0.03 (1)	0.01 (0)	8.63 (71)	0.14 (1)	49.32 (57)	0.08 (1)	0.40 (3)		99.8 (5)	91.06 (79)
smol12	4	41.45 (13)		0.04 (1)	0.02 (0)	8.27 (12)	0.13 (2)	49.62 (18)	0.09 (1)	0.39 (3)		99.6 (4)	91.45 (14)
intol1	10	41.30 (29)		0.04 (2)	0.03 (2)	8.32 (9)	0.14 (2)	49.67 (21)	0.11 (2)	0.41 (3)		99.7 (5)	91.41 (10)
intol2	19	41.17 (29)	0.01 (2)	0.04 (2)	0.02 (1)	9.18 (14)	0.13 (2)	48.96 (20)	0.1 (1)	0.39 (3)		99.7 (5)	90.47 (16)
intol3	19	41.35 (39)		0.02 (1)	0.02 (0)	8.37 (17)	0.12 (2)	49.67 (24)	0.07 (1)	0.39 (3)		100.1 (9)	91.37 (16)
intol4	3/**3**	40.51 (27)		0.01 (2)	**0.023 (2)**	9.97 (20)	**0.148 (2)**	48.87 (14)	**0.069 (1)**	**0.382 (8)**	**0.004 (4)**	99.3 (3)	89.73 (18)
intol5	4/**3**	40.80 (39)	0.01 (1)	0.01 (1)	**0.022 (1)**	8.81 (26)	**0.128 (2)**	49.68 (31)	**0.070 (1)**	**0.401 (5)**	**0.007 (2)**	99.6 (8)	90.96 (22)
intol6	2/**3**	40.85 (63)	0.01 (1)	0.01 (2)	**0.021 (2)**	8.74 (36)	**0.131 (1)**	49.74 (21)	**0.066 (0)**	**0.393 (11)**	**0.009 (1)**	99.5 (6)	91.03 (31)
intol7	3/**3**	40.59 (34)		0.02 (1)	**0.027 (1)**	8.62 (29)	**0.138 (3)**	50.05 (15)	**0.089 (3)**	**0.370 (7)**	**0.008 (2)**	99.1 (4)	91.19 (27)
intol8	5/**3**	40.25 (20)	0.01 (1)	0.02 (1)	**0.014 (2)**	9.90 (20)	**0.155 (4)**	49.08 (13)	**0.073 (1)**	**0.382 (8)**	**0.007 (1)**	99.2 (9)	89.83 (20)
larol1	43/**24**	40.84 (55)		**0.030 (2)**	**0.006 (8)**	10.17 (20)	**0.147 (2)**	48.22 (47)	**0.093 (9)**	**0.388 (14)**	**0.010 (3)**	99.8 (8)	89.42 (20)
larol2	65/**17**	41.16 (70)		**0.029 (2)**	**0.004 (15)**	8.44 (23)	**0.136 (3)**	49.89 (75)	**0.084 (3)**	**0.371 (10)**	**0.007 (2)**	100.0 (10)	91.33 (20)
larol3	53/**15**	41.29 (111)		**0.022 (1)**	**0.007 (4)**	8.67 (29)	**0.129 (2)**	49.35 (93)	**0.076 (19)**	**0.400 (12)**	**0.012 (8)**	99.7 (8)	91.02 (23)
111,312/44[b]	44/**23**	40.46 (74)		**0.029 (16)**	**0.015 (3)**	9.65 (36)	**0.144 (6)**	49.12 (55)	**0.093 (6)**	**0.379 (18)**	**0.011 (5)**	100.5 (12)	90.1 (3)

All compositions are normalized to a sum of 100%. When NiO was not analysed, it was assumed at 0.40 wt% for the normalization. Original analytical totals are reported in the column "Total".
Concentrations in bold were acquired with the 2-step high current analyses (see Table S1).
The error (in parentheses) is the two standard deviation and is given in terms of the least unit cited (e.g., 41.17 (22) represents 41.17 ± 0.22 wt%, and 41.1 (22) represents 41.1 ± 2.2 wt%).
[a] number of analyses per grain; when two numbers are given (e.g. 4/3), the second, in bold, is the number of analyses performed to obtain the concentrations of selected trace elements (in bold) using the high-current setup; the fisrt is the number of analyses performed for the other elements.
[b] USNM San Carlos reference material 111312/44.
[c] Fo (%) = Mg/(Mg + Fe)*100, in mol. %.

using laser ablation inductively coupled plasma mass spectroscopy (LA-ICP-MS). Analyses were performed at the University of Utah on a Teledyne-Photon Machines Analyte Excite Excimer Laser Ablation system attached to an Agilent 8900 ICP-MS. The laser fluence was set at 0.47 J/cm^2. The laser carrier and the nebulizer gas flow were 1 L He/min (0.4 L/min cup +0.6 L/min cell) and 1.1 L Ar/min, respectively. We performed three analyses per individual grain and two analyses per grain from the selected xenoliths to allow mineral compositional variability to be assessed. Large individual grains, xenolith grains and NMNH 111312/42 grains were acquired with lines of 300 μm. Beam diameter and sample translations rates were 110 and 80 μm and 4 and 12 μm/s for individual grains, and for USNM reference material and xenoliths grains, respectively. Small individual grain compositions were acquired with spot analyses (110 μm). The choice of large spot size follows recommendations by Bussweiler et al. (2019) who showed fractionation effects in high-Mg olivine become especially problematic at spot sizes <75 μm. We used a laser operating at 10 Hz frequency and each analysis was preceded by a cleaning shot. Acquisition times were about 50s for analyses on the small non-USNM grain, the reference material and the xenolith grains, and about 2 min 40s on the large grains. LA-ICP-MS data were treated with Excel. Each signal was carefully monitored for any spikes or an increase in signals of certain elements such as Ba and Sr which may indicate the presence of cracks or inclusions, in which case the analysis was discarded. For analyses performed on the USNM reference material and on xenoliths, we analyzed both ^{63}Cu and ^{65}Cu to check for interference between ^{63}Cu and

Table 2
Average LA-ICP-MS analyses on each separate olivine grain.

	smol1	smol2	smol3	smol4	smol5	smol6	smol7	smol8
Li	1.96 (2)	2.19 (7)	2.06 (15)	1.91 (12)	2.10 (22)	2.65 (9)	1.95 (6)	1.91 (7)
P	9.6 (6)	80.4 (22)	24.4 (25)	52.8 (28)	5.4 (3)	37.6 (59)	9.7 (6)	9.4 (7)
Ca	583 (12)	604 (4)	597 (13)	594 (5)	580 (8)	566 (20)	574 (6)	571 (12)
Ti	14.7 (10)	7.2 (4)	7.4 (3)	18.3 (11)	5.5 (4)	10.3 (3)	7.8 (2)	4.2 (5)
V	3.83 (3)	2.95 (4)	3.25 (7)	4.00 (2)	3.27 (12)	2.98 (8)	3.38 (3)	3.16 (7)
Mn	902 (12)	1083 (11)	1078 (15)	1142 (13)	1005 (76)	1166 (21)	994 (14)	1047 (34)
Zn	78.3 (7)	78.4 (12)	74.7 (34)	79.7 (10)	77.6 (59)	80.7 (32)	75.8 (22)	71.7 (16)
Sc	3.91 (5)	4.20 (7)	4.07 (8)	4.07 (1)	4.02 (9)	4.35 (8)	4.07 (2)	4.19 (6)
Cr	137.3 (35)	138.9 (6)	136.9 (26)	75.7 (8)	147.0 (94)	140.1 (40)	132.8 (28)	129.5 (30)
Co	187 (3)	181 (12)	183 (2)	198 (2)	182 (11)	175 (6)	179 (4)	177 (4)
Ni	3327 (63)	3139 (34)	3294 (79)	2797 (38)	3241 (181)	3003 (120)	3207 (86)	3248 (102)
Cu	1.14 (4)	2.34 (10)	4.34 (10)	1.15 (5)	1.38 (8)	2.23 (5)	1.79 (38)	5.11 (12)
Ga	0.049 (6)	0.036 (4)	0.034 (2)	0.056 (2)	0.035 (2)	0.046 (4)	0.036 (1)	0.028 (3)
Ge	1.27 (2)	1.30 (2)	1.33 (14)	1.71 (5)	1.27 (30)	1.30 (9)	1.14 (14)	1.25 (8)
	smol9	smol10	smol11	smol12	larol1	larol2	larol3	111312/42[a]
Li	1.83 (2)	2.46 (6)	1.96 (15)	1.91 (7)	3.73 (4)	2.44 (24)	1.88 (9)	1.47 (49)
P	27.6 (13)	49.4 (114)	5.6 (11)	17.9 (27)	38.8 (72)	29.1 (33)	4.1 (5)	24.4 (41)
Ca	581 (15)	561 (8)	576 (11)	582 (9)	610 (43)	599 (37)	534 (3)	683 (144)
Ti	12.5 (12)	14.9 (4)	3.1 (3)	1.7 (3)	42.4 (3)	23.0 (18)	17.0 (13)	23.1 (54)
V	4.12 (2)	3.29 (3)	3.82 (7)	3.82 (5)	4.13 (8)	4.53 (16)	3.65 (5)	4.44 (66)
Mn	1030 (26)	1093 (26)	1066 (15)	994 (13)	1029 (86)	1083 (73)	881 (38)	1115 (20)
Zn	68.1 (49)	75.3 (26)	77.4 (8)	70.8 (11)	81.9 (79)	68.9 (74)	61.9 (24)	60.4 (17)
Sc	4.17 (5)	4.00 (9)	4.07 (3)	4.16 (6)	4.02 (43)	3.39 (37)	3.51 (16)	3.24 (125)
Cr	156.7 (16)	98.9 (13)	179.2 (17)	245.6 (52)	303.9 (180)	265.1 (177)	157.5 (46)	104.9 (41)
Co	173 (4)	179 (3)	173 (4)	170 (3)	176 (15)	174 (13)	156 (6)	140 (3)
Ni	3184 (90)	3233 (59)	3171 (45)	3188 (46)	3112 (299)	3248 (250)	2842 (107)	2767 (62)
Cu	1.20 (13)	1.24 (2)	0.97 (2)	1.34 (2)	3.09 (33)	4.86 (36)	4.15 (15)	0.85 (21)
Ga	0.035 (4)	0.037 (3)	0.034 (1)	0.033 (2)	0.069 (6)	0.064 (3)	0.031 (1)	0.053 (8)
Ge	1.14 (7)	1.40 (12)	1.22 (1)	1.12 (3)	1.38 (46)	1.14 (33)	0.83 (11)	1.41 (62)

We performed 3 analyses per grain. For a given grain, the error is the largest value between 2 standard deviations and the analytical error.
The error (in parentheses) is the two standard deviation and is given in terms of the least unit cited (e.g, 1.96 (2) represents 1.96 ± 0.02 ppm, and 583 (12) represents 583 ± 12 ppm).
When only one analysis was selected, the error is the single point analytical sensitivity.
[a] San Carlos reference material NMNH 111312/42.

$^{23}Na^{40}Ar$. The good correspondence between the two signals rules out interference issues (Fig. S1a). However, signal analyses for Cu show extreme intragrain variability not observed in any other elements. We interpret these strong signals in Cu as the presence of inclusions of sulfides. The fact that these inclusions only affect Cu signal is likely due to the very low Cu concentrations in olivine in comparison to other elements usually present in sulfides inclusions (i.e., Fe and Ni, Savelyev et al., 2018). We discarded the part of the signal corresponding to the inclusion, when possible (i.e., sharp peak in the signal, easy to isolate; Fig. S1b), or the entire analysis when necessary (heterogenous signal with no single peak that can be discarded). We used the silicate glass standard NIST 610 for Ni and Mn and NIST 612 for all other elements as reference material. The olivine Si contents, measured by electron microprobe, served as an internal standard. We tested the accuracy of the measurement with BCR-2G as an external standard with analysis every 4 to 6 analyses. The measured concentrations are compared with concentrations obtained by Gao et al. (2002) with LA-ICP-MS. Based on 60 BRC-2G measurements, the relative errors on the trace element contents lie between 0.2 and 15% (Table S2).

4. Results

4.1. Method validity

Precision and accuracy of the Mn, Zn, Ca, Cr and Ni measurements were independently checked by comparing results obtained with both analytical techniques on a selection of grains. Fig. 1 shows that concentrations measured for Mn, Zn and Ni using the electron microprobe fit with those analyzed by LA-ICP-MS. Cr and Ca contents show slightly more variability but most analyses fall within two standard deviations.

In Fig. 2 we compare the compositions of the SC olivines performed in this study with SC olivine analyses from previous studies and mantle olivines from other locations (Wang et al., 2021). All analyses performed in this study on individual grains and on peridotite xenoliths show high forsterite contents (Fo > 88). Compositions of olivine in pyroxenitic samples are significantly more variable with forsterite content varying from 68.9 to 90.1.

4.2. Comparison between non-USNM San Carlos olivines and USNM material

Average electron microprobe (EPMA) and LA-ICP-MS analyses per separate grain are listed in Tables 1 & 2, respectively. EPMA individual analyses can be found in Table S3. The purpose of this study is not to provide a comprehensive study of the composition of the USNM San Carlos material, but rather to highlight the compositional variability that can exist in non-USNM San Carlos olivine.

4.2.1. Major and minor elements

Major- and minor-element zoning in large individual grains are nearly absent, demonstrating chemical equilibrium in the samples (Fig. 3). However, the compositional overlap between each grain is limited. The profiles in Fig. 3, obtained with the 2-step analysis setup, also highlight the importance of using high current for minor elements; discrimination between the MnO contents of these grains is not possible using MnO profiles obtained with one-step analysis (Fig. S2). This is also seen in Fig. 4 which compares the distribution of the minor elements (NiO, MnO, Al_2O_3 and CaO) obtained on the USNM reference material 111312/44 using the one-step and the two-step procedure. The range of MnO and CaO concentrations obtained from the 2-step procedure is more restricted.

The USNM reference material analyzed in this study shows a restricted range of Fo content (90.1 ± 0.3; Fig. 2), consistent with Fournelle's analyses (2011) (90.1 ± 0.2). The SiO_2 content varies from

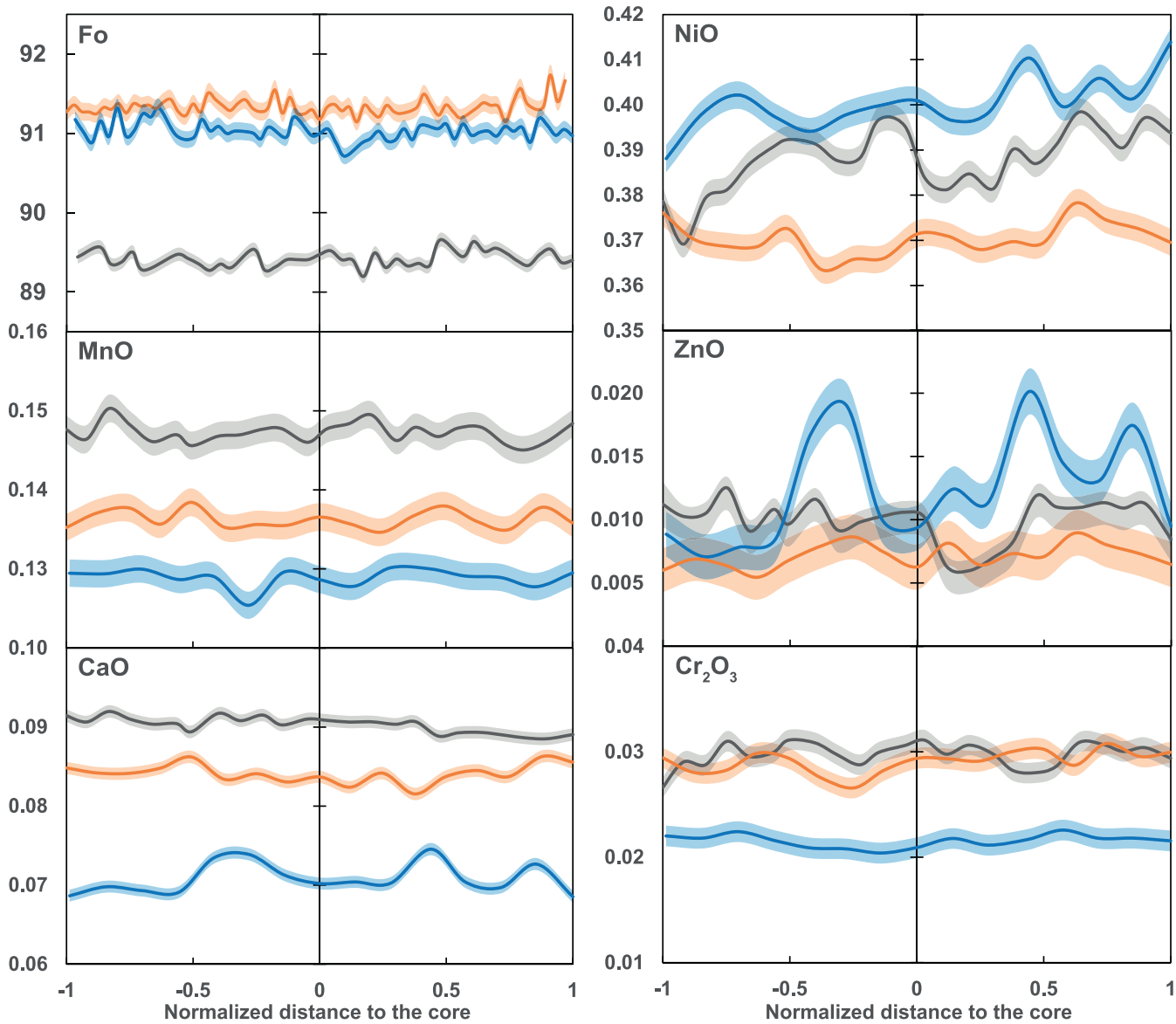

Fig. 3. Compositional profiles in three large non-USNM San Carlos grains (each color corresponds to a different grain). Spatial resolution is 100 μm for forsterite content (Fo, in %), 200 μm for the oxides (in wt%). The shaded area around each profile represents ±2AE (i.e., Analytical Error).

39.8 to 41.2 wt% with an average of 40.3 ± 0.7 (2σ) wt%, well overlapping with the value reported in Jarosewich et al. (1980) (i.e, 40.81 wt %). This is also consistent with Fournelle's analysis that reported a wider range of heterogeneity in Si and Mg than originally published in Jarosewich and coworker report (1980). The Boyd homogeneity index (Boyd et al., 1967) for Si reported by Fournelle on 71 measurements on 23 grains of USNM111312/44 is 2.32 versus 0.81 in Jarosewich et al. (1980) obtained with 100 measurements performed on 10 grains. Remarkably, the average contents for minor elements obtained with the one-step and the two-step procedure both fit with the average contents reported in the literature (Fig. 4). However, even when using the two-step high current setting, the concentration obtained from a single-grain analysis can fall outside of the range of concentration reported from the literature, supporting Jarosewich and Fournelle's conclusions that an individual grain of USNM San Carlos olivine cannot be assumed as having the published composition, even when the published standard deviation is taken into account.

In comparison, the non-USNM SC olivines (1) cover a larger range of compositions and (2) do not systematically match the composition of the reference material. The concentration distributions in the individual grains show an offset toward higher Fo, SiO_2 and NiO contents (Figs. 2,4), and lower CaO (and MnO) contents (Fig. 4) in comparison to USNM 111312/44. Finally, Al_2O_3 shows a bimodal distribution both in USNM and non-USNM material, suggesting the existence of two populations of San Carlos olivine. The range of Al_2O_3 obtained on the USNM material in this study is larger than the range reported in EPMA analyses in the literature and plotted in Fig. 4 (see Table S5a), but is consistent with the range of concentrations reported by De Hoog et al. (2010) obtained by LA-ICP-MS analyses (see Table S5b). As for the other elements, the covered range is however much larger in the non-USNM material than in the reference material, extending both toward lower and higher concentrations, and with more than an order of magnitude between the lowest and highest concentrations (Table 1). This heterogeneity is important because Al partitioning between olivine and spinel has become a widely used thermometer (e.g. Coogan et al., 2014; Matthews et al., 2021 and reference therein).

4.2.2. *Trace elements*

Published trace element compositions for USNM San Carlos olivine are relatively limited (see Table S5b).

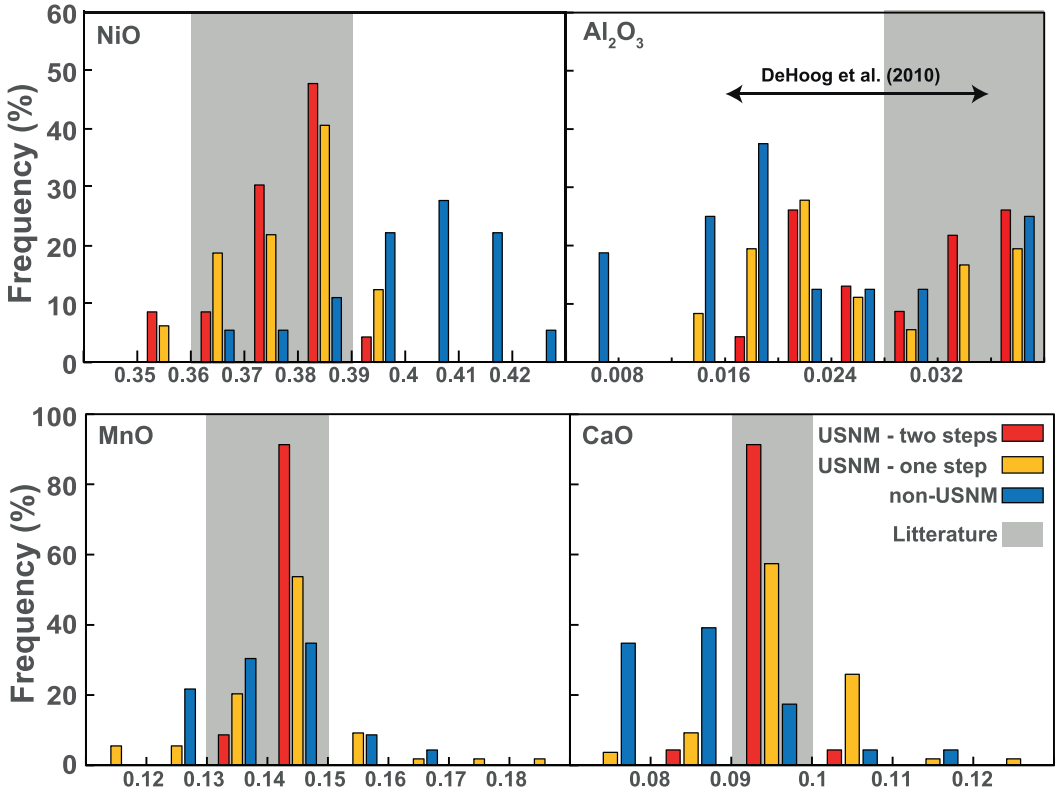

Fig. 4. NiO (wt%), MnO (wt%), Al_2O_3 (wt%) and CaO (wt%) concentration distributions obtained on all the single analyses performed on the USNM 111312/44 material (yellow) and on single analyses performed only with the two-step high-current procedure (red) (see text for detail and Table S3), compared with the distribution of the average concentrations of non-USNM SC individual grains (blue) reported in this study (Table 1). The shaded area represents the range of average USNM reference material compositions reported in the literature (see Table S5a). For the Al_2O_3 distribution, the range reported byDe Hoog et al. (2010) is also plotted (see Table S5b). (For interpretation of the references to colour in this figure legend, the reader is referred to the web version of this article.)

Fig. 5 presents the primitive mantle (PM)-normalized concentrations of FRTE (First Row Transition Elements), Ga, Ge, P and Li in individual grains, compared with concentrations acquired on NMNH 111312/42, a split of the USNM San Carlos material specifically prepared for trace element analyses, provided by the Smithsonian Institute. Olivine grains have near-PM abundances of Li, Ge, Mn, Zn, Co, Ni, and negative anomalies at Ti, Ga, Cu, V, Sc, Ti, Cr and P.

In comparison to the reference material, the non-USNM SC olivines are usually depleted in Ti, Ga and V and enriched in Cu, Li, Zn, Co and Ni. P concentrations show high variability, from <5 to >80 ppm.

4.3. Olivines in pyroxenite xenoliths

Average electron microprobe (EPMA) of mineral phases from xenoliths are listed in Table 3. EPMA individual analyses on xenolith minerals can be found in Table S4. LA-ICP-MS analyses on olivine from xenoliths are listed in Table 4.

4.3.1. Major and minor elements

Mineral chemistry in peridotite and pyroxenite xenoliths is consistent to a first order with the petrographic description of the samples. Forsterite content increases from SC1 to SC4 and SC2-3B (Fig. 2). While the Mg# of the pyroxenes are correlated with the Fo contents of the associated olivines, all clinopyroxenes analyzed in this study fall in the diopside field using the Ca–Fe–Mg pyroxene classification (Fig. S3). Al_2O_3 and TiO_2 decrease and Cr_2O_3 increases with increasing Mg#. Na_2O contents are relatively constant (Fig. 6). Using the two-pyroxene barothermometer from Putirka (2008) on the pyroxenite xenoliths, we obtained remarkably small ranges of pressures (6.8–7.8 kbar) and temperatures (1025–1045 °C) of equilibration. If we include xenoliths containing only one pyroxene, the temperature range expands to 985–1100 °C when assuming the mean pressure of 7.3 kbar. Because of the relatively small ranges of pressures and temperatures obtained in this study, *P-T* variations are unlikely to be responsible for the observed compositional variations.

4.3.2. Trace elements

Fig. 7 presents selected trace elements in olivine from xenoliths compared with concentration in individual grains of olivine and reference material analyzed in this study, ranked in a crescent order of Fo contents. Trace elements show general trends with Li, P, Zn and, to a lesser extent, Co decreasing, and Ni, Cr and Mn increasing with increasing Fo. The olivines from the clinopyroxenites SC5A, SC3–1 and SC3–2 have distinctly lower Ni and Cr than the olivines from the websterite SC2–1 and the harzburgite SC5B that present concentrations similar to those recorded in the individual olivine grains and the USNM reference material. However, SC2–1 olivines present intermediate P and Mn concentrations between the olivine clinopyroxenites, and the harzburgite and olivine grains. SC2–1 olivines also present slightly higher concentrations in Li than SC3–1&2 olivines.

5. Discussion

5.1. Variability of San Carlos olivine as starting material

San Carlos olivines are commonly used as starting materials in melt-rock reactions experiments, or diffusion and partitioning experiments. Individual grains of San Carlos olivine appear to be homogeneous and do not present systematic zoning patterns. Hence, any olivine zonation observed after experiments using SC olivine can be interpreted as a result of the experiment (e.g., Borghini et al., 2018; Spandler and O'Neill, 2010; Van Den Bleeken et al., 2010; Zhang et al., 2018).

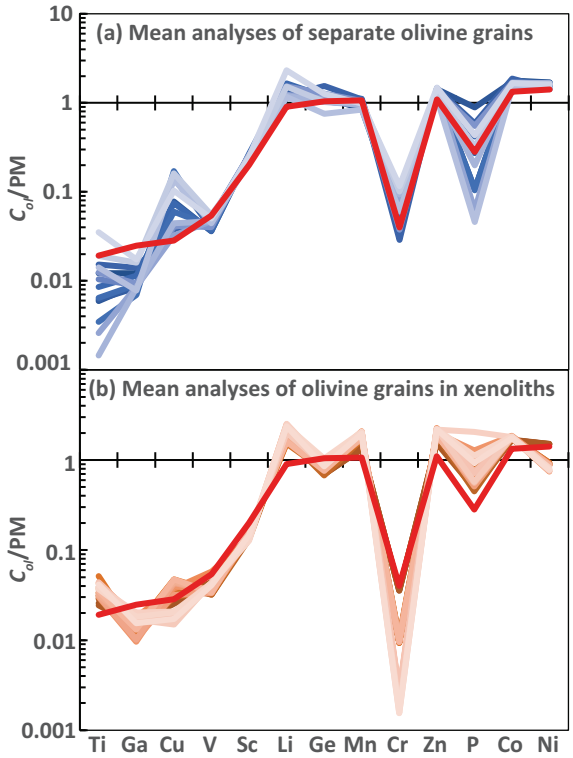

Fig. 5. Primitive mantle-normalized average concentrations of FRTE, Ga, Ge, Li and P of individual grains of San Carlos olivine (blue shading (a)) and of olivine grains from xenoliths (orange shading (b)) compared with the concentration of the NMNH 111312/42 reference material (red). Elements are ordered based on increasing olivine/melt partitioning coefficients using the recommended values of Le Roux et al. (2015) for the FRTE, Ga, and Ge, and a value of 0.29 for Li (Spandler and O'Neill, 2010) and a value of 1 for P (Shea et al., 2019). Primitive mantle values are from McDonough and Sun (1995).

However, this study also demonstrates that San Carlos olivine composition is not fixed and does not necessarily match the composition of the USNM reference material. For instance, the USNM reference material shows lower Co, Zn and Ni concentrations than any individual grains we analyzed in this study (Fig. 7). In addition, there is no systematic correlation between major, minor and trace elements: in Fig. 3, the gray profile shows that the grain with the lowest Fo content presents intermediate NiO contents. Similarly, the orange profile presents the highest Fo content, but intermediate CaO, Cr_2O_3 and MnO contents. In Fig. 7, despite the general trends observed amongst the xenoliths, there is no correlation between the Fo content and the trace elements concentration amongst the individual olivine grains. Two of the large grains commercially acquired show significantly higher Cr contents than the rest of the grains.

The variability of San Carlos olivine in some major (e.g., Fo content) and minor (e.g., Ni and Ca) elements has been taken into account in previous experimental studies (e.g., Borghini et al., 2018; Van Den Bleeken et al., 2010), but with the recent gain in interest in using trace elements in mantle olivine as tracers of petrogenetic processes (e.g., De Hoog et al., 2010; Foley et al., 2013; Jean et al., 2016; Mallmann et al., 2009; Rasmussen et al., 2020; Wang et al., 2021), we would like to encourage future experimental studies to also consider the San Carlos variability in trace elements. As our contribution, Table 5 reports the ranges of concentrations in olivine for the elements analyzed in this study to provide some guidance for future experimental studies.

5.2. Origin of olivine pyroxenites in San Carlos

Olivines from xenoliths cover a large range of Fo contents (68–92%). Following Frey and Prinz's classification (1978), SC2-3B, SC4w-h and SC5B have forsterite contents consistent with Group 1 xenoliths (i.e., mantle origin), olivine from SC1 and SC5A are consistent with Group 2 xenoliths (i.e. cumulative origin), and olivines from SC3–1, SC3–2, SC2–1, and SC2-3A present intermediate Fo. The analyses of trace elements in olivine may shed some new light on the origin of the olivine pyroxenites. The increase in incompatible elements (e.g., Ti, P) and the variations of Ni and Mn with Fo (Fig. 7) are consistent with a differentiation trend (e.g., Sobolev et al., 2005, 2007). Based on this preliminary information, we could consider that SC2-3A to SC1 (Fig. 2) form a suite of cumulative rocks, SC1 being the most differentiated end of the trend. However, all olivine analyses in this study present low Ti (< 60 ppm; Fig. 7) and Ca (< 500 ppm; Fig. S4) contents, consistent with a mantle origin (Foley et al., 2013). Additionally, all clinopyroxenes show constant Na_2O content (Fig. 6). This differs from a typical differentiation trend that results in increases in both Ti and Na contents (Fig. S5, e.g., Villiger et al., 2004).

Melt-rock reactions in the mantle have been described in many studies and result in either the production of olivine at the expense of orthopyroxene (e.g., Daines and Kohlstedt, 1994; Jackson and Gibson, 2018; Kelemen, 1990; Morgan and Liang, 2003; Pilet et al., 2008), or the production of orthopyroxene at the expanse of olivine (e.g., Yaxley and Green, 1998; Mallik and Dasgupta, 2012). Lambart et al. (2012) demonstrated that the type of the reaction mostly depends on the silica activity of the melt in comparison to the activity of a melt in equilibrium with both solid phases, but also pointed out that if the reactions happen beneath the solidus of the rock host, they will both result in a strong precipitation of clinopyroxene.

We argue that SC2–1, SC2-3A, and SC4-w are the result of melt-rock reaction between the peridotite host (spinel lherzolite) and a basaltic melt resulting in the dissolution of olivine and the precipitation of orthopyroxene and clinopyroxene, following the reaction:

$$\text{Liq } 1 + \text{olivine} -> \text{Liq } 2 + \text{opx} + \text{cpx} \quad (1)$$

SC2–1, SC2-3A, and SC4-w have Ni contents similar to the Ni contents in the peridotite xenoliths (SC5-B and SC2-3B) and in the individual grains of olivine (Fig. 7 and Fig. S4). While fractionation results in a strong decrease of the olivine Ni content, dissolution of olivine during melt-rock reaction should result in increasing the Ni content of the residual olivine (e.g., Kelemen et al., 1998; Milke et al., 2011). Laukert et al. (2014) did similar observations on a series of websterites associated with harzburgites from the ultraslow-spreading Lena Trough (Arctic Ocean). Olivine from both websterite and harzburgite present the same Ni content and cannot be explained if the replacement of olivine by pyroxene proceeded in equal proportions. They suggested that the reaction must result in a mass ratio of precipitated pyroxene to dissolved olivine (Mpx/Mol) greatly higher than 1. This is consistent with Lambart et al. (2012) which showed that the reaction of a basaltic andesite (P40–15) with peridotite below the solidus of the peridotite results in Mpx/Mol ~ 2. Ni is also a fast diffusive element (e.g., Petry et al., 2004) and may have been partly reequilibrated with the peridotite host, especially if the reaction was associated with the large volume of melt (see below; e.g., Jackson and Gibson, 2018).

Melt-rock reaction such as described in reaction (1) is usually accompanied by a decrease in the Fo content of the olivine, consistent with our observations for SC2–1 and SC2-3A (Fig. 2). SC4-w however, despite being largely dominated by pyroxene (Fig. 8) shows Fo content very similar to the associated harzburgite (SC4-h). Composite samples such as SC4h-w have been recently proposed as resulting from

Table 3
Average of electron microprobe analyses on the mineral phases in each xenolith.

Sample#[a]	Phase	n[b]	SiO_2	TiO_2	Al_2O_3	Cr_2O_3	FeO	MnO	MgO	CaO	Na_2O	NiO	ZnO	P_2O_5	Total	Mg#[c]
SC1	olivine	16	37.0 (4)	0.03 (1)	0.08 (8)		27.8 (7)	0.35 (4)	34.6 (4)	0.12 (1)		0.06 (3)			99.9 97)	68.9 (7)
cpxite	cpx	16	47.7 (5)	1.8 (2)	8.5 (6)	0.03 (1)	7.5 (2)	0.18 (3)	13.0 (3)	20.4 (5)	0.89 (9)	0.05 (1)			99.9 (7)	75.5 (7)
	spinel	8	0.042 (3)	0.67 (7)	60.4 (5)	0.14 (2)	24.7 (8)	0.16 (2)	13.8 (4)			0.11 (5)			99.9 (7)	50 (1)
SC2–1	olivine	13	39.5 (14)	0.02 (2)	0.01 (1)	0.02 (2)	14.8 (76)	0.19 (8)	45.0 (62)	0.07 (2)	0.00 (1)				100.3 (10)	84.4 (88)
ol-web	opx	32	53.7 (5)	0.16 (5)	4.4 (3)	0.49 (7)	8.5 (3)	0.18 (4)	31.4 (5)	0.96 (37)	0.09 (2)				100.1 (9)	86.8 (4)
	cpx	5	51.0 (7)	0.60 (16)	6.23 (46)	0.98 (10)	3.88 (27)	0.10 (2)	15.83 (21)	20.07 (11)	1.31 (9)				99.2 (9)	87.9 (7)
SC2-3A	olivine	10	39.9 (3)	0.02 (1)	0.08 (1)		13.5 (2)	0.18 (2)	45.9 (4)	0.08 (1)		0.40 (4)			100.5 (9)	85.8 (3)
ol-web	opx	33	54.2 (4)	0.19 (3)	4.2 (3)	0.50 (11)	8.3 (2)	0.18 (3)	31.4 (4)	0.92 (5)	0.09 (2)	0.11 (3)			101.0 (7)	87.1 (4)
	cpx	1	51.1 (1)	0.75 (2)	6.29 (3)	0.98 (2)	3.63 (5)	0.13 (1)	15.60 (3)	20.16 (4)	1.32 (2)	0.06 (2)			100.4	88.5
	spinel	6	0.15 (1)	0.36 (4)	48.9 (24)	17.5 (23)	15.6 (5)	0.11 (4)	17.2 (4)			0.36 (4)			99.7 (6)	66.3 (12)
SC2-3B	olivine	10	40.8 (3)	0.02 (1)	0.03 (1)	0.03 (2)	8.4 (3)	0.14 (3)	50.1 (3)	0.08 (1)	0.01 (1)	0.39 (6)			100.8 (8)	91.4 (3)
harz																
SC3–1	olivine	53	39.2 (6)	0.06 (14)	0.05 (6)	0.01 (2)	17.5 (8)	0.24 (4)	42.9 (5)	0.07 (9)		0.23 (5)			99.8 (10)	81.4 (8)
ol-cpxite	ol (HC)	11	38.9 (3)			**0.004 (3)**	17.9 (6)	**0.233 (59)**	42.7 (5)	**0.055 (22)**		**0.230 (63)**	**0.012 (8)**	**0.018 (12)**	100.2 (8)	81.0 (6)
	cpx	36	49.6 (8)	1.1 (3)	7.2 (7)	0.7 (2)	5.0 (3)	0.14 (3)	14.5 (4)	20.6 (4)	1.17 (9)	0.06 (1)			99.8 (15)	83.9 (9)
	spinel	4	0.1 (0)	0.40 (11)	55.7 (7)	8.2 (4)	18.9 (5)	0.15 (3)	16.6 (2)			0.28 (3)			99.1 (9)	61.0 (5)
	Kaersutite	5	41.9 (4)	6.0 (18)	11.0 (34)	0.9 (4)	4.8 (13)	0.06 (4)	12.3 (16)	22.3 (13)	0.7 (2)				100.7 (6)	83 (4)
SC3–2	olivine	39	38.8 (7)	0.02 (2)	0.02 (2)	0.01 (2)	17.6 (25)	0.24 (4)	43.1 (19)	0.06 (1)					100.1 (10)	81.3 (28)
ol-cpxite	ol (HC)	13	38.7 (2)		**0.012 (2)**	**0.004 (2)**	17.8 (3)	**0.244 (7)**	42.9 (3)	**0.061 (4)**		**0.245 (6)**	**0.013 (4)**	**0.022 (12)**	100.3 (9)	81.1 (4)
	cpx	17	48.9 (6)	1.04 (24)	7.24 (80)	0.69 (15)	5.1 (2)	0.14 (3)	14.5 (5)	20.4 (3)	1.17 (9)				99.2 (8)	83.7 (6)
	spinel	3	0.03 (1)	0.32 (6)	56.0 (3)	7.5 (3)	19.2 (4)	0.13 (4)	16.6 (2)						99.8 (6)	60.7 (4)
SC4-h	olivine	31	40.7 (4)	0.01 (3)	0.01 (2)	0.02 (2)	9.3 (3)	0.14 (3)	49.7 (4)	0.07 (1)					100.1 (6)	90.5 (3)
harz																
	ol (HC)	10	40.4 (3)		**0.015 (3)**	**0.014 (2)**	9.3 (3)	**0.134 (23)**	49.6 (4)	**0.066 (5)**		**0.407 (8)**	**0.007 (3)**	**0.008 (2)**	100.4 (6)	90.5 (3)
	opx	5	54.8 (4)	0.12 (4)	3.7 (2)	0.55 (4)	5.7 (2)	0.15 (5)	34.0 (5)	0.84 (5)	0.07 (1)				100.7 (14)	91.3 (3)
	spinel	2	0.02 (2)	0.22 (0)	44.9 (7)	23.4 (7)	12.6 (0)	0.13 (3)	18.7 (0)		0.01 (1)				98.6 90)	72.5 (1)
SC4-w	olivine	9	40.7 (5)	0.02 (2)	0.01 (2)	0.01 (1)	9.5 (4)	0.14 (3)	49.6 (5)	0.07 (1)					99.7 (6)	90.3 (4)
web																
	ol (HC)	4	40.5 (6)		**0.016 (2)**	**0.013 (3)**	9.4 (4)	**0.140 (5)**	49.4 (5)	**0.065 (3)**		**0.402 (4)**	**0.008 (3)**	**0.008 (2)**	100.1 (8)	90.3 (4)
	opx	10	54.4 (8)	0.14 (6)	4.3 (7)	0.54 (7)	6.0 (3)	0.14 (3)	33.5 (4)	0.85 (9)	0.08 (4)				100.4 (6)	90.8 (5)
	cpx	6	51.6 (6)	0.46 (9)	5.6 (11)	0.98 (31)	2.8 (1)	0.09 (3)	16.6 (4)	20.9 (2)	1.08 (7)				99.7 (5)	91.5 (5)
	spinel	3	0.04 (2)	0.22 (4)	48.6 (16)	19.7 (15)	12.1 (4)	0.09 (2)	19.2 (2)						98.7 (4)	73.9 (7)
SC5-A	olivine	31	37.6 (6)	0.02 (2)	0.01 (2)	0.00 (1)	24.1 (8)	0.29 (4)	37.8 (5)	0.07 (2)	0.01 (2)				100.2 (8)	73.7 (8)
ol-cpxite																
	ol (HC)	10	37.6 (6)		**0.013 (3)**	**0.021 (1)**	24.0 (8)	**0.293 (10)**	37.7 (4)	**0.071 (4)**		**0.199 (22)**	**0.015 (6)**	**0.021 (13)**	100.3 (8)	73.7 (8)
	cpx	9	48 (1)	1.33 (35)	8.3 (17)	0.20 (32)	6.5 (4)	0.16 (4)	13.7 (8)	20.3 (5)	1.2 (2)				99.4 (10)	79 (1)
	spinel	4	0.02 (3)	0.28 (6)	61.5 (8)	1.35 (36)	21.1 (7)	0.12 (2)	15.6 (3)						100.3 (7)	57 (1)
SC5-B	olivine	11	40.5 (4)	0.02 (2)	0.01 (0)	0.02 (1)	9.1 (1)	0.13 (2)	49.7 (4)	0.07 (2)	0.02 (0)				99.6 (7)	90.6 (2)
harz	ol (HC)	2	40.4 (3)		**0.013 (1)**	**0.014 (3)**	9.2 (0)	**0.136 (11)**	49.8 (3)	**0.069 (7)**		**0.408 (6)**	**0.008 (4)**	**0.009 (3)**	100.2 (8)	90.6 (1)
	opx	2	55.0 (4)	0.08 (3)	3.1 (1)	0.59 (2)	5.8 (5)	0.15 (3)	34.3 (1)	0.9 (1)					100.4 (10)	91.3 (10)
	cpx	1	52.4 (1)	0.17 (3)	3.9 (8)	1.10 (22)	2.5 (5)	0.096 (2)	17.45 (3)	21.64 (4)	0.72 (14)				100.2	92.502867
	spinel	3	0.05 (1)	0.16 (6)	37.6 (6)	31.1 (4)	13.8 (1)	0.11 (4)	17.2 (1)	0.01 (0)					98.7 (10)	68.9 (2)

All compositions are normalized to a sum of 100%. When NiO was not analysed, it was assumed at 0.40 wt% for the normalization. Original analytical totals are reported in the column "Total".
The error (in parentheses) is the two standard deviation and is given in terms of the least unit cited (e.g., 37.0 (4) represents 37.0 ± 0.4 wt%, and 0.03 (1) represents 0.03 ± 0.01 wt%).
When only one analysis is performed ($n = 1$), the error is the the single point analytical sensitivity.

[a] *lithologies*: cpxite = an olivine and spinel bearing clinopyroxenite; ol-cpxite = olivine clinopyroxenite; web = websterite; ol-web = olivine websterite; harz = harzburgite.

[b] n = number of analyses (individual analyses are reported in Table S4); ol (HC): minor concentrations (in bold) were obtained with the 2-steps set up (Table S1).

[c] Mg# = Mg/(Mg + Fe) *100, in mol. %, assuming all Fe is Fe^{2+}.

Table 4
Average of LA-ICP-MS analyses (in ppm) on the olivines in xenoliths.

	SC2–1 (olivine websterite)			SC3–1 (olivine clinopyroxenite)					SC3–2 (olivine clinopyroxenite)				*
Li	3.27 (23)	3.30 (19)	3.33 (39)	2.95 (22)	2.83 (9)	3.22 (6)	2.69 (8)	2.57 (3)	2.72 (26)	2.81 (20)	2.83 (47)	2.89 (45)	2.43 (0)
P	59.2 (15)	64.0 (12)	43.4 (153)	114.7 (401)	45.9 (51)	88.3 (529)	50.3 (68)	50.2 (227)	64.7 (108)	40.3 (10)	93.1 (732)	93.9 (126)	68.9 (0)
Ca	456 (4)	449 (8)	445 (7)	405 (2)	426 (29)	396 (5)	397 (23)	409 (57)	389 (41)	375 (21)	395 (15)	397 (51)	401 (0)
Ti	34.7 (24)	31.0 (5)	29.3 (16)	36.6 (12)	39.4 (12)	36.9 (6)	38.1 (25)	42.2 (49)	37.9 (59)	35.1 (16)	40.3 (23)	46.8 (27)	44.6 (0)
V	3.15 (13)	3.33 (13)	3.62 (1)	2.80 (7)	2.74 (8)	2.84 (9)	2.92 (8)	2.76 (4)	2.62 93)	2.62 (2)	2.68 (6)	2.94 (14)	2.85 (0)
Mn	1419 (63)	1397 (1)	1382 (27)	1940 (15)	1886 (60)	1866 (1)	1823 (57)	1856 (24)	1757 (22)	1776 (71)	1743 (86)	1798 (86)	1808 (1)
Zn	86.4 (5)	83.6 (2)	84.1 (45)	110.1 (12)	107.7 (70)	106.0 (39)	103.2 (79)	104.2 (11)	101.5 (13)	101.9 (49)	100.8 (58)	106.8 (45)	106.5 (0)
Sc	2.30 (19)	2.32 (5)	2.33 (0)	2.30 (8)	2.47 (11)	2.28 (19)	2.40 (9)	2.59 (40)	2.31 (38)	2.14 (12)	2.41 (26)	2.26 (24)	2.46 (0)
Cr	92.7 (29)	93.9 (16)	94.6 (20)	25.7 (11)	25.7 (6)	25.0 (12)	26.0 (10)	25.2 (5)	24.7 (2)	25.2 (2)	24.5 (6)	25.5 (4)	27.3 (0)
Co	174 (7)	176 (2)	174 (0)	195 (4)	188 (7)	187 (3)	186 (9)	187 (1)	181 (0)	183 (0)	180 (3)	186 (7)	185 (0)
Ni	2942 (117)	2961 (36)	2960 (12)	1764 (74)	1703 (51)	1736 (27)	1707 (82)	1742 (12)	1724 (15)	1769 (14)	1730 (41)	1823 (2)	1764 (0)
Cu	0.96 (2)	0.76 (32)	0.87 (10)	1.20 (0)	0.95 (10)	1.30 (0)	1.33 (10)	1.42 (39)	1.33 (14)	1.21 (3)	1.20 (40)	0.90 (0)	1.06 (1)
Ga	0.055 (11)	0.061 (11)	0.058 (6)	0.039 (3)	0.041 (2)	0.040 (19)	0.057 (5)	0.052 (18)	0.053 (1)	0.043 (9)	0.049 (6)	0.046 (10)	0.051 (0)
Ge	0.89 (12)	0.76 (13)	0.76 (5)	1.03 (9)	0.88 (9)	0.87 (5)	0.87 (3)	0.83 (3)	0.82 (2)	0.81 (10)	0.74 (8)	0.98 (13)	0.85 (0)
	SC3–2 (*continued*)			SC5-A (olivine clinopyroxenite)							SC5-B (harzburgite)		
Li	2.78 (17)	2.47 (13)	2.81 (36)	3.98 (53)	3.40 (20)	3.30 (3)	3.23 (5)	4.04 (50)	3.80 (27)	3.79 (31)	1.41 (9)	1.44 (21)	
P	51.2 (108)	54.2 (17)	100.3 (757)	58.8 (213)	66.8 (59)	64.5 (282)	51.2 (65)	184.8 (306)	100.4 (86)	84.0 (520)	17.0 (0)	15.7 (12)	
Ca	383 (32)	394 (35)	396 (27)	468 (36)	453 (35)	450 (53)	451 (37)	419 (14)	430 (1)	455 (64)	427 (18)	423 (5)	
Ti	37.2 (109)	43.7 (71)	40.5 (28)	51.6 (45)	52.9 (33)	52.5 (38)	49.8 (77)	46.5 (4)	44.4 (8)	49.8 (89)	12.3 (11)	11.8 (3)	
V	2.71 (18)	2.74 (5)	2.90 (51)	4.74 (14)	3.55 (8)	3.47 (15)	3.56 (5)	3.53 (4)	3.52 (1)	3.35 (10)	3.17 (20)	3.24 (3)	
Mn	1805 (130)	1814 (89)	1787 (112)	2177 (4.5)	2144 (64)	2141 (32)	2145 (71)	2120 (3)	2141 (24)	2054 (19)	1017 (67)	1050 (28)	
Zn	109.1 (90)	106.2 (86)	106.6 (40)	124.9 (51)	122.6 (4)	120.4 (4)	121.0 (54)	119.8 (24)	120.7 (38)	120.6 (20)	51.7 (12)	53.5 (14)	
Sc	2.30 (56)	2.40 (32)	2.29 (9)	2.22 (17)	2.26 (27)	2.23 (36)	2.26 (30)	2.19 (60	2.06 (24)	2.38 (35)	3.14 (23)	2.89 (18)	
Cr	24.6 (21)	27.8 (36)	24.7 (6)	6.92 (10)	5.34 (41)	7.27 (28)	4.74 (11)	4.44 (20)	4.09 (5)	4.06 (39)	103.6 (49)	105.9 (1)	
Co	190 (19)	182 (8)	182 (6)	187 (2)	191 (6)	187 (4)	190 (0)	188 (2)	192 (2)	183 (4)	134 (4)	138 (2)	
Ni	1829 (185)	1759 (76)	1751 (50)	1459 (3)	1482 (2)	1488 (43)	1543 (6)	1525 (21)	1599 (4)	1517 (28)	2876 (90)	2971 (35)	
Cu	1.41 (14)	1.36 (18)	1.42 (37)	1.12 (0)	0.50 (0)	0.57 (1)	0.45 (18)	0.62 (5)	0.61 (13)	0.52 (39)	4.32 (4)	4.38 (12)	
Ga	0.055 (11)	0.048 (3)	0.056 (17)	0.072 (3)	0.070 (18)	0.070 (3)	0.068 (11)	0.081 (4)	0.073 (4)	0.062 (4)	0.027 (13)	0.021 (8)	
Ge	1.06 (29)	0.95 (13)	0.84 (25)	0.93 (8)	1.01 (19)	0.97 (6)	0.97 (12)	1.00 (0)	1.14 (5)	0.94 (4)	0.66 (9)	0.68 (1)	

The error (in parentheses) is the two standard deviation and is given in terms of the least unit cited (e.g., 3.27 (23) represents 3.27 ± 0.23 ppm, and 59.2 (15) represents 59.2 ± 1.5 ppm).
* only one analysis was performed on this grain, the error is the single-analysis analytical error.

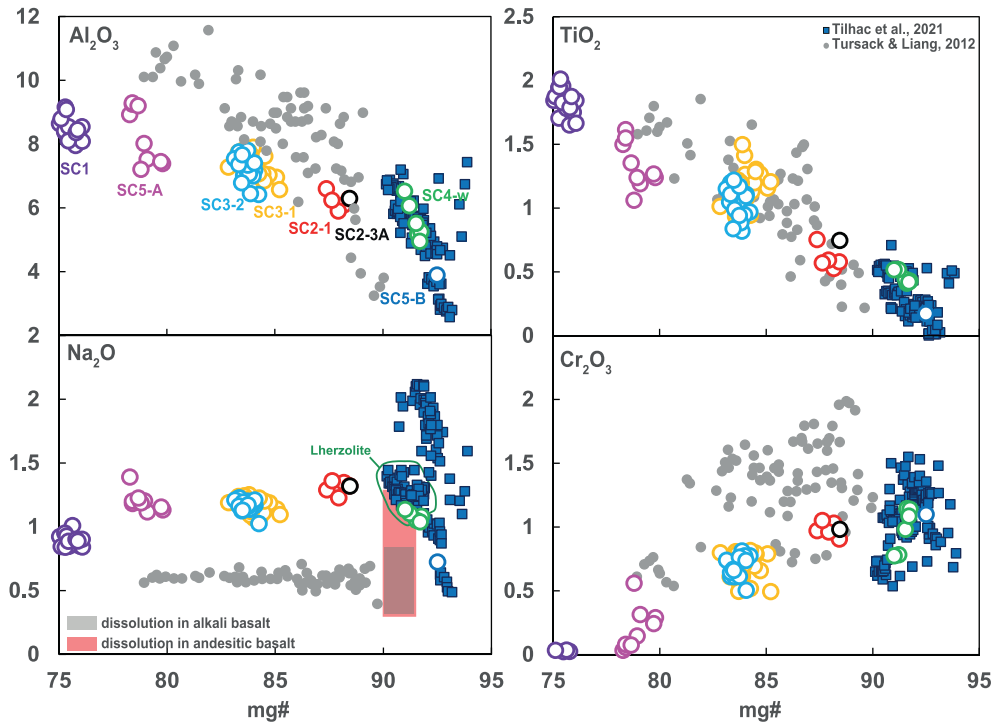

Fig. 6. Composition of the clinopyroxenes analyzed in the xenoliths in (wt%). Compositions are compared with the cpx from lherzolite and harzburgite xenoliths from San Carlos studied by Tilhac et al. (2021), and with the cpx produced with the lherzolite dissolution in an alkali basalt followed by progressive cooling (Tursack and Liang, 2012). In the plot Na_2O vs Mg#, the gray and the red square represent the range of cpx compositions obtained from lherzolite dissolution (without step cooling) in the same alkali basalt (Morgan and Liang, 2003) and in a basaltic andesite (Morgan and Liang, 2005), respectively. (For interpretation of the references to colour in this figure legend, the reader is referred to the web version of this article.)

metamorphic segregation (Tilhac et al., 2021). The authors argued that the homogeneous Na_2O contents and similarly LREE-depleted patterns observed in pyroxenes from both lithologies suggest their formation must be related. Additionally, in their study, no significant chemical variation was observed across the contact, suggesting an isochemical process.

Fig. 8 presents the compositional variability at the contact between an harzburgite (SC4-h) and an olivine websterite (SC4-w). Olivine does not show any compositional variation between the two lithologies. However, both pyroxenes in the olivine websterite (SC4-w) show an increase of their Mg# and a significant decrease of their Al_2O_3 content at the contact with the harzburgite, inconsistent with an isochemical process. We argue that SC4-w is also the product of reaction (1); the olivine in the websterite is residual while pyroxenes are precipitated during the reaction. The new precipitated pyroxenes have a lower Mg# and higher Al_2O_3 content and tends to reequilibrate in contact with the harzburgite. The limited range of compositional variation however suggests that the reaction might have been accompanied by a mineral segregation process to result in a rapid increase of the proportion of pyroxene in SC4-w and a rapid decrease of their proportion in SC4-h. Unlike Tilhac et al. (2021) however, who documented mineral segregation occurring mostly through metamorphic deformation with only a small amount of liquid present, we suggest that, in this case, the mineral segregation was favored by a high melt/rock ratio. This is also consistent with the limited intragrain variability observed in SC4-w (Table 3). In fact, Jackson and Gibson (2018) showed that in the presence of a low melt/rock ratio, melt-rock reaction results in olivines recording Ni (and Cr) disequilibrium, decoupled from Fo. On the contrary, a magma/rock ratio promotes full reequilibration. A similar scenario was proposed by Frey and Prinz (1978) and Wilshire and Shervais (1975) who considered precipitation and flow differentiation of pyroxenes along the edges of a feeder dike (i.e., pathway with a high melt-rock ratio) to explain the petrographic and geochemical characteristics of such composite sample. Finally, Denis et al. (2018) studied a websterite-dunite composite sample and showed that the crystal preferred orientations of olivine and pyroxene in such composite samples are not consistent with a single deformation event. They suggested that the websterite was formed by the addition of pyroxene at the expense of the dunite assemblage, consistently with reaction (1). The authors further argued that a secondary melting stage could explain the LREE-depleted patterns of the pyroxenes (Frey and Prinz, 1978; Denis et al., 2018; Tilhac et al., 2021) and the low water concentration measured in both olivine and pyroxene (Denis et al., 2018) in such composite samples.

We further argue that segregation and in situ crystallization of residual melt (i.e., liq 2) from reaction (1) can produce the xenoliths SC1, SC5A, SC3-1 and SC3-2. The high phosphorous intragrain variability for these is consistent with a magmatic origin (e.g., Milman-Barris et al., 2008; Shea et al., 2019). The low Ni and Cr contents of the olivine in these xenoliths are consistent with precipitation from a melt (Fig. 7). The slight increase of Co with decreasing Fo is also consistent with a fractionation effect (Herzberg et al., 2016). Preferential dissolution of olivine and precipitation of pyroxenes will result in decreasing the silica and MgO concentrations of the melt, consistently with the correlation between the low mg# and the low SiO_2 content in the olivine (Fig. 2). It can also explain why olivine keep low Ca and Ti contents (i.e., mantle values) as both elements are incorporated into pyroxene.

Finally, in Fig. 6, we compare the composition of the clinopyroxenes from our study with the compositions obtained by Tursack and Liang (2012) in dissolution experiments followed by step-cooling. We consider general compositional trends rather than absolute values and ranges, as the latter also depend on temperature, pressure, and reacting melt and peridotite compositions (Wang et al., 2013). Despite the higher content in Na_2O observed in natural samples, the cpx reprecipitated from the residual hybrid melt after by melt-peridotite reaction reproduce the general trend observed in the suite of xenoliths, and in particular, the decoupled behavior between the two incompatible elements Ti and Na. It is also worth noting that the low Na_2O content in Tursack and Liang (2012) were obtained in experiments where the peridotite reacts with an alkali basalt, resulting in the dissolution of pyroxenes and precipitation of olivine. On the contrary, peridotite dissolution experiments in a basaltic andesite resulted in the precipitation of opx and the expense of olivine and clinopyroxene (Morgan and Liang, 2005). The initial range of Na_2O from the clinopyroxenes (i.e., before cooling) obtained in these experiments expands towards higher concentration (Fig. 6). Hence,

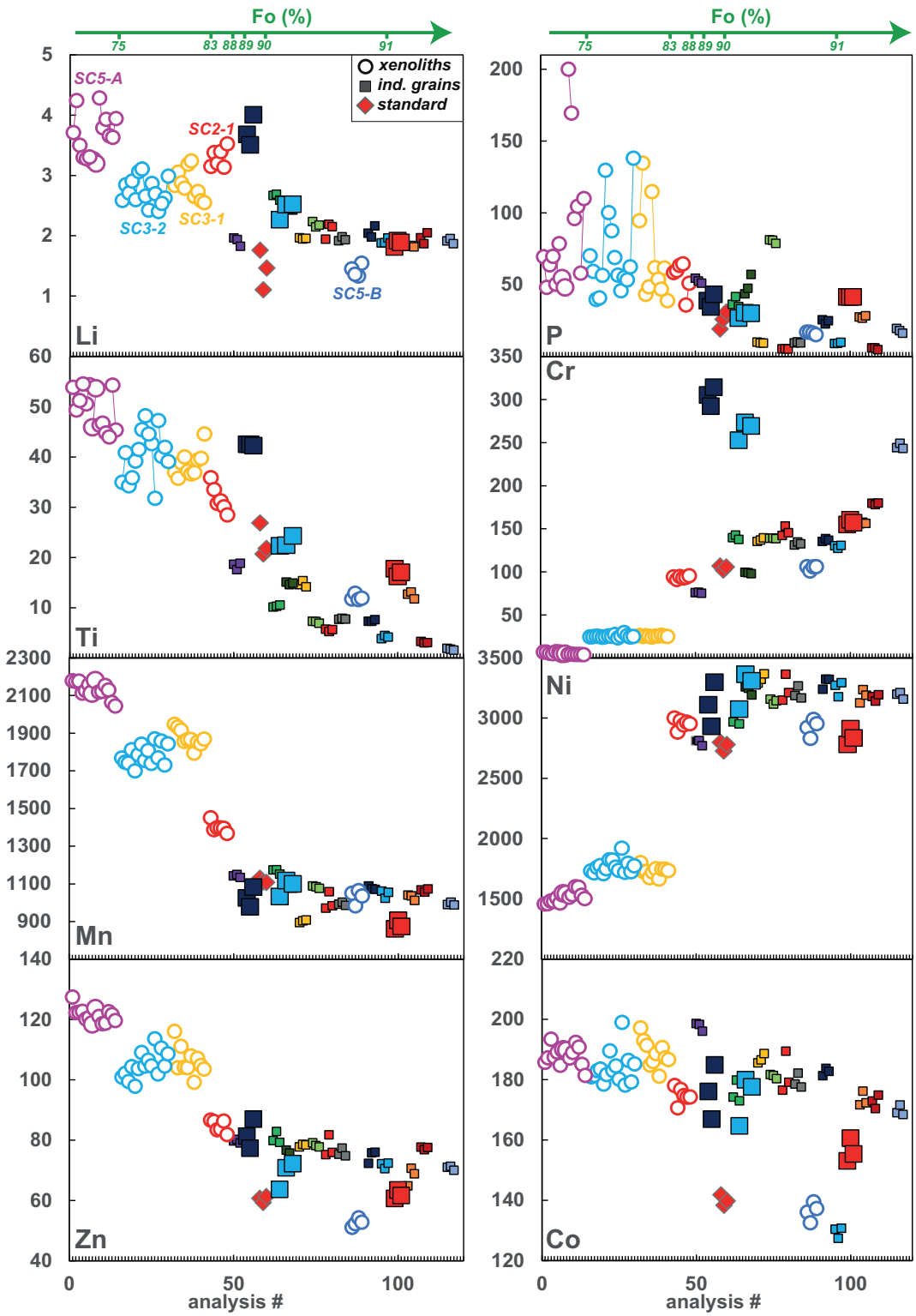

Fig. 7. Elements concentrations (in ppm) measured in every single LA-ICP-MS analysis performed in this study. For analyses performed on xenoliths (open circles; each color corresponds to a different xenolith), analyzed from the same grains are connected by solid lines. For analyses performed on individual grains (squares; each color corresponds to a different xenolith), the larger squares refer to the three large olivine crystals. Analyses on NMNH 111312/42 reference material are represented by red diamonds.

Table 5
Range of concentrations in the non-USNM San Carlos olivines analyzed in this study.

	all		Fo > 89.9	
	min	max	min	max
SiO_2	36.7	41.8	40.1	41.8
Al_2O_3	0.00	0.23	0	0.23
FeO	8.0	28.3	8	9.8
MnO	0.095	0.39	0.095	0.173
MgO	34.2	50.3	48	50.3
CaO	0.05	0.13	0.06	0.123
NiO	0.05	0.44	0.35	0.44
Li	1.1	4.3	1.1	2.5
P	4.8	200	4.8	81.3
Ti	1.6	54.5	1.6	26.9
Cr	3.9	314	102	314
Zn	51	127	51	83
Co	127	199	127	189
Sc	1.94	4.4	2.8	4.4
V	2.61	4.8	2.94	4.64
Cu	0.32	4.44	0.95	5.17
Ga	0.02	0.08	0.02	0.06
Ge	0.62	1.72	0.62	1.47

Oxides are in wt%, elements are in ppm.

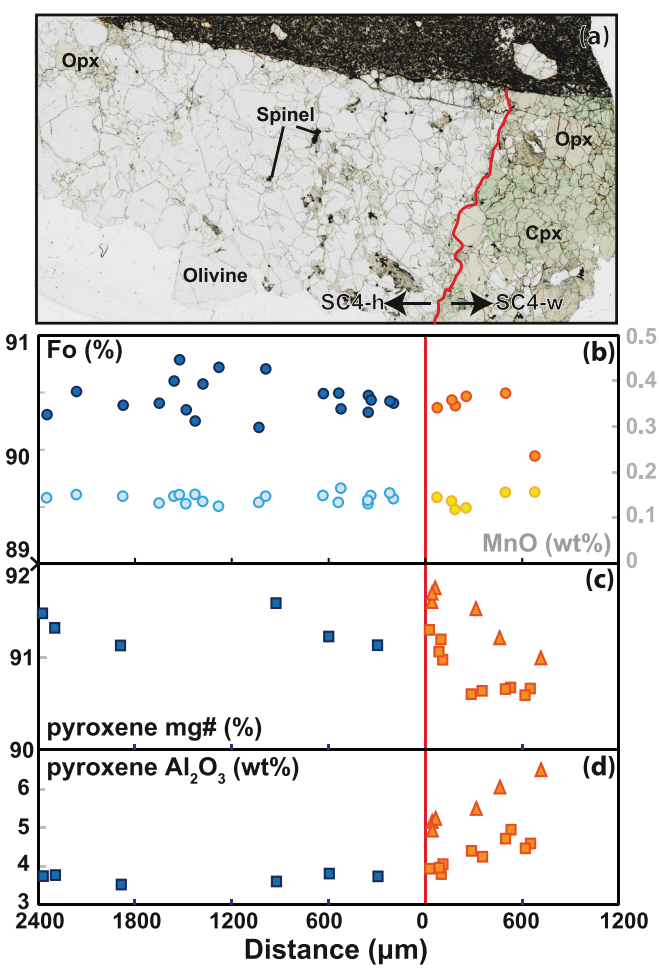

Fig. 8. (a) Thin section picture and (b-d) compositional profiles across the composite sample SC4h-w. (b) Fosterite (Fo) (dark symbols) and MnO (light symbols) contents in olivine. (c-d) Mg# and Al_2O_3 contents in opx (square) and cpx (triangle).

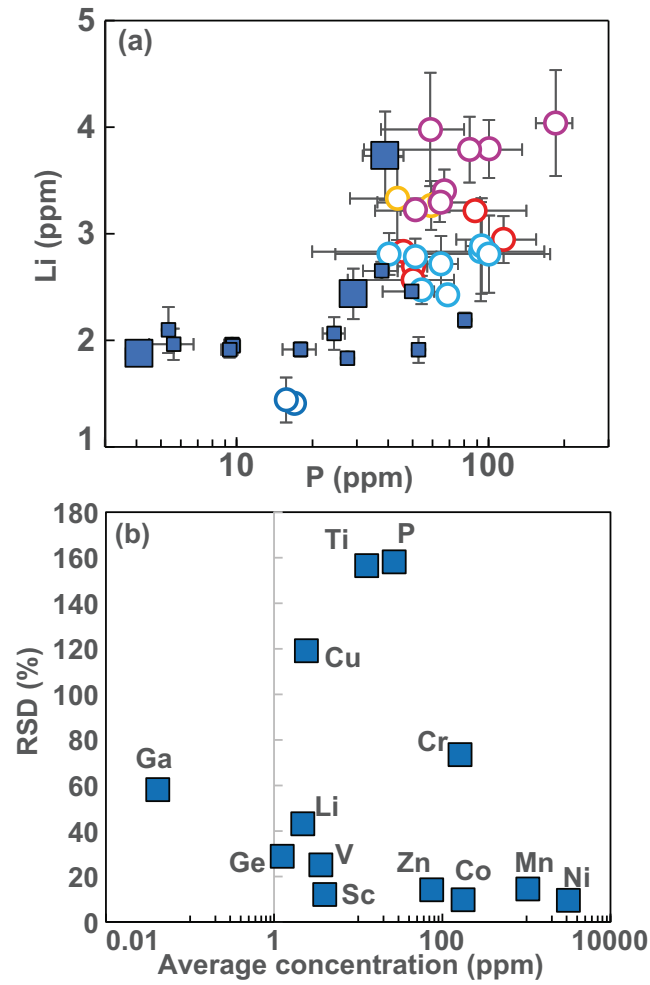

Fig. 9. (a) Li vs P concentrations (in ppm) in all non-USNM olivine grains. Squares are mean concentrations obtained on individual olivine grains, the three large squares represent the three large olivine grains. Open circles are mean concentrations obtained on olivine from xenoliths (same color code than in Fig. 7). Error bars are two standard deviations obtained from analyses performed on the same grain. (b) Relative variability (RSD = 2SD/Average concentration) of the concentrations between the individual grains as a function of the average concentration in the olivine grains for each element. RSD for each xenolith are plotted in Fig. S6.

progressive cooling of such experiments would likely produce cpx with higher Na_2O content than those reported in Tursack and Liang (2012)'s experiments.

5.3. P variability

While the main goal of this contribution is to provide constraints on the compositional variability of San Carlos olivine, here we briefly discuss the implications for the high variability in P contents observed in the olivine (Fig. 9). High variability of P in olivine is commonly observed in magmatic olivine (Milman-Barris et al., 2008) and is usually attributed to rapid growth of olivine (e.g., Welsch et al., 2014; Shea et al., 2019). We interpret the larger intragrain variability observed in SC5A, SC3–1 and SC3–2 as resulting from this process (Fig. 7). High variability in P has also been reported in peridotite xenoliths from Australia (e.g., Woodland et al., 2004; Mallmann et al., 2009) and was attributed to secondary metasomatic episodes. In fact, Woodland et al. (2004) showed

that P enrichment is usually associated with Li enrichment. In our samples, SC2–1, interpreted as the result of melt-rock reaction is enriched in both elements (Fig. 9a). It is noteworthy that one of the large grains of olivine commercially acquired is even more enriched in Li than olivine from SC2–1, suggesting that this grain was also likely affected by melt-rock reaction or by a metasomatic event. However, the majority of the individual grains analyzed in this study show relatively constant Li concentration (around ~2 ppm) for a large range of P contents (~ 4 to 55 ppm). Additionally, the absence of correlation between the relative variability of the elements and their average concentration (Fig. 9b) demonstrate that observed variability is not due to the analytical error. The contrasted behavior between P and Li, two incompatible elements, may be due to their different diffusion behavior: P is one of the slowest diffusing element (Watson et al., 2015), while Li is a fast-diffusion cation (e.g., Dohmen et al., 2010). However, we still need to understand the incorporation of P in mantle olivine.

Because of its high charge and very small ionic radius, phosphorus is generally inferred to occupy the tetrahedral site and substitute for Si (e.g., Agrell et al., 1998; Boesenberg et al., 2004). Several mechanisms for substitution have been suggested. The main ones are vacancy in octahedral site (Boesenberg et al., 2004 and references therein) or in tetrahedral site (e.g., Agrell et al., 1998; Self and Buseck, 1983), and the coupled substitution of $^{IV}Si^{4+}$ and $^{VI}Mg^{2+}$ by $^{IV}P^{5+}$ and $^{VI}Li^{+}$,Na^{+},H^{+} (Woodland et al., 2004). Forsterite-rich grains in skarns and marbles show a Li:P enrichment factor close to 1 (Beno et al., 2020; Nekrylov et al., 2021) suggesting that, in this case, the couple substitution is the dominant process in the incorporation of P (and Li) in olivine. Mallmann et al.'s (2009) documented excellent correlations between P, Li and Na in olivine from individual xenoliths and demonstrated that crystal zoning Li (and Na) and P are correlated. This supports a role for the couple substitution mechanism, but the authors also pointed out that the slope between P^{5+} against Li^{+} in olivine per formula unit of four oxygens is <0.02 (in other words, only <2% of P^{5+} cation follow this mechanism - pure couple substitution would result in a slope of 1; see Fig. 9 in Mallmann et al., 2009). Hence, incorporation of Li in olivine is likely utilized for charge balancing, but P must mostly substitute into mantle olivine by other mechanisms. Mallmann et al. (2009) proposed that metasomatism by a P-rich fluid or melt could precipitate a rim of P-rich olivine. Subsequent sub-solidus deformation and recrystallization could redistribute P in the olivine. This is consistent with the higher P content observed in SC2–1, interpreted as resulting of a melt-rock reaction. Shea et al. (2019) showed that P partitioning between olivine depends on growth rate and varies from 0.01 to 1 with increasing rate. They further suggested that a tendency for the olivine lattice to be slightly more flexible during periods of fast growth could promote the incorporation of larger amounts of small P^{5+} cations. Hence, if P variability in mantle olivines is the result of melt circulation, it suggests that this process must be a highly dynamic and reactive to result in fast dissolution-reprecipitation of minerals.

6. Conclusions

(1) Following Fournelle's conclusions (2011), non-USNM distributed material cannot be assumed to be of the same composition as USNM 111312/444. In comparison to the reference material, non-USNM San Carlos Fo-rich olivines analyzed in this study are depleted in Ti, Ga and V and enriched in Cu, Li, Zn, Co and Ni. They also show significant variability in trace elements (e.g., P, Cu and Ti relative variability is >100%).

(2) Olivine pyroxenites associated with peridotite xenoliths likely result from melt-rock reaction: olivine-rich – Mg-rich pyroxenites are formed by dissolution of olivine and precipitation of pyroxenes from the peridotite host (i.e., mantle origin); olivine-poor – Fe-rich pyroxenites are formed by segregation of the residual melt after reaction with the peridotite and in situ crystallization (i.e., magmatic origin).

(3) P intragrain variability is interpreted as resulting of fast-crystal growth in both magmatic and mantle olivines. Fast-crystal growth in mantle olivine implies a very reactive metasomatic process.

Funding

This work was supported by the National Science Foundation (EAR-1946346) and the ACS Petroleum Research Fund (# 61305-DNI8) to S.L. and by the UROP program of the University of Utah to S.H.

Authors contributions

S.L. designed the study. S.L. wrote the manuscript with input from S.H. and O.L. S.H, O.L and S.L performed the analyses.

Data availability

All the data supporting the findings of this study are included in the manuscript or available in the supplementary material attached with this paper.

Declaration of Competing Interest

The authors declare that they have no known competing financial interests or personal relationships that could have appeared to influence the work reported in this paper.

Acknowledgments

We thank the reviewers, Valentin Batanova, Sally Gibson and John Fournelle, and the editor Catherine Chauvel, for thorough and helpful comments that greatly improved the quality of this manuscript. We thank the Smithsonian Institution National Museum of Natural History for San Carlos reference material NMNH 111312/42 and NMNH 111312/44. We also thank George Rossman for the synthetic Mn and Ni olivines used as primary standards in electron microprobe analyses. We thank Quintin Sahratian for support with sample preparation. For assistance with analytical techniques, we thank Wil Mace (EPMA), Diego Fernandez, Christopher Anderson, and Brad Munk (LA-ICPMS). We also thank Kayla Iacovino for providing some of the olivines analyzed in this study. Finally, we would like to acknowledge that the samples analyzed in this study are from The San Carlos Apache Reservation, part of the ancestral lands of the Apache People.

Appendix A. Supplementary data

Supplementary data to this article can be found online at https://doi.org/10.1016/j.chemgeo.2022.120968.

References

Agrell, S.O., Charnley, N.R., Chinner, G.A., 1998. Phosphoran olivine from Pine Canyon, Piute Co., Utah. Mineral. Mag. 62 (2), 265–269.

Beno, C.J., Bowman, J.R., Loury, P.C., Tapanila, L.M., Fernandez, D.P., 2020. Evidence for dendritic crystallization of forsterite olivine during contact metamorphism of siliceous dolostones, Alta stock aureole, Utah. Contributions to Mineralogy and Petrology 175 (10), 1–26.

Boesenberg, J.S., Ebel, D.S., Hewins, R.H., 2004. An experimental study of phosphoran olivine and its significance in main group pallasites. In: Lunar and Planetary Science Conference, p. 1366.

Borghini, G., Francomme, J.E., Fumagalli, P., 2018. Melt-dunite interactions at 0.5 and 0.7 GPa: experimental constraints on the origin of olivine-rich troctolites. Lithos 323, 44–57.

Boyd, F.R., Finger, L.W., Chayes, F., 1967. Computer reduction of electron probe data. In: Carnegie Institution of Washington Yearbook, 67, pp. 21–215.

Bussweiler, Y., Giuliani, A., Greig, A., Kjarsgaard, B.A., Petts, D., Jackson, S.E., Pearson, D.G., 2019. Trace element analysis of high-Mg olivine by LA-ICP-MS–Characterization of natural olivine standards for matrix-matched calibration and application to mantle peridotites. Chem. Geol. 524, 136–157.

Coogan, L.A., Saunders, A.D., Wilson, R.N., 2014. Aluminum-in-olivine thermometry of primitive basalts: Evidence of an anomalously hot mantle source for large igneous provinces. Chem. Geol. 368, 1–10.

Daines, M.J., Kohlstedt, D.L., 1994. The transition from porous to channelized flow due to melt/rock reaction during melt migration. Geophys. Res. Lett. 21 (2), 145–148.

De Hoog, J.C., Gall, L., Cornell, D.H., 2010. Trace-element geochemistry of mantle olivine and application to mantle petrogenesis and geothermobarometry. Chem. Geol. 270 (1–4), 196–215.

Demouchy, S., Alard, O., 2021. Hydrogen, trace, and ultra-trace element distribution in natural olivines. Contrib. Mineral. Petrol. 176 (4), 1–25.

Denis, C.M., Demouchy, S., Alard, O., 2018. Heterogeneous hydrogen distribution in orthopyroxene from veined mantle peridotite (San Carlos, Arizona): Impact of melt-rock interactions. Lithos 302, 298–311.

Dohmen, R., Kasemann, S.A., Coogan, L., Chakraborty, S., 2010. Diffusion of Li in olivine. Part I: experimental observations and a multi species diffusion model. Geochim. Cosmochim. Acta 74 (1), 274–292.

Foley, S.F., Prelevic, D., Rehfeldt, T., Jacob, D.E., 2013. Minor and trace elements in olivines as probes into early igneous and mantle melting processes. Earth Planet. Sci. Lett. 363, 181–191.

Fournelle, J., 2011. An investigation of "San Carlos Olivine": comparing USNM-distributed material with commercially available material. Microsc. Microanal. 17 (Supplement 2), 842–843.

Frey, F.A., Prinz, M., 1978. Ultramafic inclusions from San Carlos, Arizona: petrologic and geochemical data bearing on their petrogenesis. Earth Planet. Sci. Lett. 38 (1), 129–176.

Galer, S.J.G., O'nions, R. K., 1989. Chemical and isotopic studies of ultramafic inclusions from the San Carlos Volcanic Field, Arizona: a bearing on their petrogenesis. J. Petrol. 30 (4), 1033–1064.

Gao, S., Liu, X., Yuan, H., Hattendorf, B., Günther, D., Chen, L., Hu, S., 2002. Determination of forty two major and trace elements in USGS and NIST SRM glasses by laser ablation-inductively coupled plasma-mass spectrometry. Geostand. Newslett. 26 (2), 181–196.

Grant, T.B., Harlov, D.E., Rhede, D., 2016. Experimental formation of pyroxenite veins by reactions between olivine and Si, Al, Ca, Na, and Cl-rich fluids at 800 °C and 800 MPa: Implications for fluid metasomatism in the mantle wedge. Am. Mineral. 101 (4), 808–818.

Herzberg, C., Vidito, C., Starkey, N.A., 2016. Nickel–cobalt contents of olivine record origins of mantle peridotite and related rocks. Am. Mineral. 101 (9), 1952–1966.

Jackson, C.G., Gibson, S.A., 2018. Preservation of systematic Ni and Cr heterogeneity in otherwise homogeneous mantle olivine: Implications for timescales of post-metasomatism re-equilibration. Lithos 318, 448–463.

Jarosewich, E.J., Nelen, J.A., Norberg, J.A., 1980. Reference samples for electron microprobe analysis. Geostand. Newslett. 4, 43–47.

Jean, M.M., Taylor, L.A., Howarth, G.H., Peslier, A.H., Fedele, L., Bodnar, R.J., Sobolev, N.V., 2016. Olivine inclusions in Siberian diamonds and mantle xenoliths: Contrasting water and trace-element contents. Lithos 265, 31–41.

Kelemen, P.B., 1990. Reaction between ultramafic rock and fractionating basaltic magma I. Phase relations, the origin of calc-alkaline magma series, and the formation of discordant dunite. J. Petrol. 31 (1), 51–98.

Kelemen, P.B., Hart, S.R., Bernstein, S., 1998. Silica enrichment in the continental upper mantle via melt/rock reaction. Earth Planet. Sci. Lett. 164 (1–2), 387–406.

Kinzler, R.J., Grove, T.L., 1992. Primary magmas of mid-ocean ridge basalts 1. Experiments and methods. Journal of Geophysical Research: Solid. Earth 97 (B5), 6885–6906.

Lambart, S., Laporte, D., Provost, A., Schiano, P., 2012. Fate of pyroxenite-derived melts in the peridotitic mantle: thermodynamic and experimental constraints. J. Petrol. 53 (3), 451–476.

Laukert, G., Von Der Handt, A., Hellebrand, E., Snow, J.E., Hoppe, P., Klügel, A., 2014. High-pressure reactive melt stagnation recorded in abyssal pyroxenites from the ultraslow-spreading Lena Trough, Arctic Ocean. J. Petrol. 55 (2), 427–458.

Le Roux, V., Dasgupta, R., Lee, C.T.A., 2015. Recommended mineral-melt partition coefficients for FRTEs (Cu), Ga, and Ge during mantle melting. Am. Mineral. 100 (11–12), 2533–2544.

Mallik, A., Dasgupta, R., 2012. Reaction between MORB-eclogite derived melts and fertile peridotite and generation of ocean island basalts. Earth Planet. Sci. Lett. 329, 97–108.

Mallmann, G., O'Neill, H.S.C., Klemme, S., 2009. Heterogeneous distribution of phosphorus in olivine from otherwise well-equilibrated spinel peridotite xenoliths and its implications for the mantle geochemistry of lithium. Contrib. Mineral. Petrol. 158 (4), 485–504.

Matthews, S., Wong, K., Shorttle, O., Edmonds, M., Maclennan, J., 2021. Do olivine crystallization temperatures faithfully record mantle temperature variability? Geochem. Geophys. Geosyst. 22 (4) e2020GC009157.

McDonough, W.F., Sun, S.S., 1995. The composition of the Earth. Chem. Geol. 120 (3–4), 223–253.

Milke, R., Abart, R., Keller, L., Rhede, D., 2011. The behavior of Mg, Fe, and Ni during the replacement of olivine by orthopyroxene: experiments relevant to mantle metasomatism. Mineral. Petrol. 103 (1–4), 1–8.

Milman-Barris, M.S., Beckett, J.R., Baker, M.B., Hofmann, A.E., Morgan, Z., Crowley, M. R., Stolper, E., 2008. Zoning of phosphorus in igneous olivine. Contrib. Mineral. Petrol. 155 (6), 739–765.

Morgan, Z., Liang, Y., 2003. An experimental and numerical study of the kinetics of harzburgite reactive dissolution with applications to dunite dike formation. Earth Planet. Sci. Lett. 214 (1–2), 59–74.

Morgan, Z., Liang, Y., 2005. An experimental study of the kinetics of lherzolite reactive dissolution with applications to melt channel formation. Contrib. Mineral. Petrol. 150 (4), 369–385.

Nekrylov, N., Plechov, P.Y., Gritsenko, Y.D., Portnyagin, M.V., Shcherbakov, V.D., Aydov, V.A., Garbe-Schönberg, D., 2021. Major and trace element composition of olivine from magnesian skarns and silicate marbles. American Mineralogist: Journal of Earth and Planetary Materials 106 (2), 206–215.

Petry, C., Chakraborty, S., Palme, H., 2004. Experimental determination of Ni diffusion coefficients in olivine and their dependence on temperature, composition, oxygen fugacity, and crystallographic orientation. Geochim. Cosmochim. Acta 68, 4179–4188.

Pilet, S., Baker, M.B., Stolper, E.M., 2008. Metasomatized lithosphere and the origin of alkaline lavas. Science 320 (5878), 916–919.

Pouchou, J.L., Pichoir, F., 1991. Quantitative analysis of homogeneous or stratified microvolumes applying the model "PAP". In: Electron probe quantitation. Springer, Boston, MA, pp. 31–75.

Putirka, K.D., 2008. Thermometers and barometers for volcanic systems. Rev. Mineral. Geochem. 69 (1), 61–120.

Rasmussen, M.B., Halldórsson, S.A., Gibson, S.A., Guðfinnsson, G.H., 2020. Olivine chemistry reveals compositional source heterogeneities within a tilted mantle plume beneath Iceland. Earth Planet. Sci. Lett. 531, 116008 https://doi.org/10.1016/j.epsl.2019.116008.

Savelyev, D.P., Kamenetsky, V.S., Danyushevsky, L.V., Botcharnikov, R.E., Kamenetsky, M.B., Park, J.W., Zelenski, M.E., 2018. Immiscible sulfide melts in primitive oceanic magmas: Evidence and implications from picrite lavas (Eastern Kamchatka, Russia). American Mineralogist: Journal of Earth and Planetary Materials 103 (6), 886–898.

Self, P.G., Buseck, P.R., 1983. High-resolution structure determination by ALCHEMI. In: Proceedings of the 41st Annual Meeting of the Electron Microscopy Society of America. San Francisco Press, pp. 178–181.

Shea, T., Hammer, J.E., Hellebrand, E., Mourey, A.J., Costa, F., First, E.C., Melnik, O., 2019. Phosphorus and aluminum zoning in olivine: contrasting behavior of two nominally incompatible trace elements. Contrib. Mineral. Petrol. 174 (10), 1–24.

Sobolev, A.V., Hofmann, A.W., Sobolev, S.V., Nikogosian, I.K., 2005. An olivine-free mantle source of Hawaiian shield basalts. Nature 434 (7033), 590–597.

Sobolev, A.V., Hofmann, A.W., Kuzmin, D.V., Yaxley, G.M., Arndt, N.T., Chung, S.L., Danyushevsky, L.V., Elliott, T., Frey, F.A., Garcia, M.O., Gurenko, A.A., Kamenetsky, V.S., Kerr, A.C., Krivolutskaya, N.A., Matvienkov, V.V., Nikogosian, I. K., Rocholl, A., Sigurdsson, I.A., Sushchevskaya, N.M., Teklay, M., 2007. The amount of recycled crust in sources of mantle-derived melts. Science 316, 412–417. https://doi.org/10.5800/gt-2012-3-1-0059.

Spandler, C., O'Neill, H.S.C., 2010. Diffusion and partition coefficients of minor and trace elements in San Carlos olivine at 1,300 C with some geochemical implications. Contrib. Mineral. Petrol. 159 (6), 791–818.

Su, C., Liu, Y., Song, W., Fan, D., Wang, Z., Tang, H., 2018. Thermodynamic properties of San Carlos olivine at high temperature and high pressure. Acta Geochimica 37 (2), 171–179.

Su, B., Chen, Y., Mao, Q., Zhang, D., Jia, L.H., Guo, S., 2019. Minor elements in olivine inspect the petrogenesis of orogenic peridotites. Lithos 344, 207–216.

Tilhac, R., Morishita, T., Hanaue, N., Tamura, A., Guotana, J.M., 2021. Systematic LREE enrichment of mantle harzburgites: The petrogenesis of San Carlos xenoliths revisited. Lithos 396, 106195.

Tursack, E., Liang, Y., 2012. A comparative study of melt-rock reactions in the mantle: laboratory dissolution experiments and geological field observations. Contrib. Mineral. Petrol. 163 (5), 861–876.

Van Den Bleeken, G., Müntener, O., Ulmer, P., 2010. Reaction processes between tholeiitic melt and residual peridotite in the uppermost mantle: An experimental study at 0· 8 GPa. J. Petrol. 51 (1–2), 153–183.

Villiger, S., Ulmer, P., Müntener, O., Thompson, A.B., 2004. The liquid line of descent of anhydrous, mantle-derived, tholeiitic liquids by fractional and equilibrium crystallization—an experimental study at 1· 0 GPa. J. Petrol. 45 (12), 2369–2388.

Wang, Z., Gaetani, G.A., 2008. Partitioning of Ni between olivine and siliceous eclogite partial melt: experimental constraints on the mantle source of Hawaiian basalts. Contrib. Mineral. Petrol. 156 (5), 661–678.

Wang, C., Liang, Y., Xu, W., Dygert, N., 2013. Effect of melt composition on basalt and peridotite interaction: laboratory dissolution experiments with applications to mineral compositional variations in mantle xenoliths from the North China Craton. Contrib. Mineral. Petrol. 166 (5), 1469–1488.

Wang, J., Su, B.X., Robinson, P.T., Xiao, Y., Bai, Y., Liu, X., Bao, Z.A., 2021. Trace elements in olivine: Proxies for petrogenesis, mineralization and discrimination of mafic-ultramafic rocks. Lithos 388, 106085.

Watson, E.B., Cherniak, D.J., Holycross, M.E., 2015. Diffusion of phosphorus in olivine and molten basalt. Am. Mineral. 100 (10), 2053–2065.

Welsch, B., Hammer, J., Hellebrand, E., 2014. Phosphorus zoning reveals dendritic architecture of olivine. Geology 42 (10), 867–870.
Wilshire, H.G., Jackson, E.D., 1975. Problems in determining mantle geotherms from pyroxene compositions of ultramafic rocks. The Journal of Geology 83 (3), 313–329.
Wilshire, H.G., Shervais, J.W., 1975. Al–augite and Cr–diopside ultramafic xenoliths in basaltic rocks from western United States. In: Physics and Chemistry of the Earth. Pergamon, pp. 257–272.
Woodland, A.B., Seitz, H.M., Yaxley, G.M., 2004. Varying behaviour of Li in metasomatised spinel peridotite xenoliths from western Victoria, Australia. Lithos 75 (1–2), 55–66.
Xu, R., Liu, Y., Lambart, S., 2020. Melting of a hydrous peridotite mantle source under the Emeishan large igneous province. Earth Sci. Rev. 207, 103253.
Yaxley, G.M., Green, D.H., 1998. Reactions between eclogite and peridotite: mantle refertilisation by subduction of oceanic crust. Schweiz. Mineral. Petrogr. Mitt. 78 (2), 243–255.
Zhang, Z., von der Handt, A., Hirschmann, M.M., 2018. An experimental study of Fe–Ni exchange between sulfide melt and olivine at upper mantle conditions: Implications for mantle sulfide compositions and phase equilibria. Contrib. Mineral. Petrol. 173 (3), 1–18.